Index 35726 X
ISSN 0867-888X

POLISH
ACADEMY
OF SCIENCES
INSTITUTE
OF FUNDAMENTAL
TECHNOLOGICAL
RESEARCH

NATIONAL
ENGINEERING
SCHOOL
OF METZ

ENGINEERING TRANSACTIONS

ROZPRAWY INŻYNIERSKIE - TRAITE d'INGENIERIE

QUARTERLY
VOLUME 61
ISSUE 2

WARSZAWA - METZ 2013

Faster online
http://et.ippt.pan.pl

Contents of issue 2 vol. LXI

Engineering Transactions, Vol. **LXI**, No. 2, pp. 85–164, Warszawa - Metz 2013

ENGINEERING TRANSACTIONS

Founded 1952
Appears since 1953

Aims and Scope

ENGINEERING TRANSACTIONS promotes research and practise in engineering science and provides a forum for interdisciplinary publications combining mechanics with material science, electronics (mechanotronics), medical science and biotechnologies (biomechanics), environmental science, photonics, information technologies and other engineering applications. The Journal publishes original papers covering a broad area of research activities including experimental and hybrid techniques as well as analytical and numerical approaches. Engineering Transactions is a quarterly issued journal for researchers in academic and industrial communities.

Address of the Editorial Office:
Engineering Transactions
Institute of Fundamental Technological Research
Pawińskiego 5B, PL 02-106 Warsaw, Poland

Phone: (48-22) 826 12 81 ext. 206, Fax: (48-22) 826 98 15, E-mail: engtrans@ippt.pan.pl

Abstracted/indexed in:

Applied Mechanics Reviews, Current Mathematical Publications, Elsevier, EMBASE, Engineering Village, Inspec, Mathematical Reviews, MathSci, Reaxys, Scopus, Zentralblatt für Mathematik.

`http://et.ippt.pan.pl/`

Address of the Editorial Office:
Engineering Transactions
Institute of Fundamental Technological Research
Pawińskiego 5B
PL 02-106 Warsaw, Poland
Phone: (48-22) 826 12 81 ext. 206, Fax: (48-22) 826 98 15
E-mail: engtrans@ippt.pan.pl

SUBSCRIPTIONS

Subscription orders for all journals edited by Institute of Fundamental Technological Research (IPPT) may be sent directly to the Publisher:
Institute of Fundamental Technological Research
e-mail: subscribe@ippt.pan.pl

Please transfer the subscription fee to our bank account:
Payee: IPPT PAN
Bank: Pekao S.A. IV O/Warszawa
Account number 05124010531111000004426875.

WARUNKI PRENUMERATY

Prenumeratę na wszystkie czasopisma wydawane przez Instytut Podstawowych Problemów Techniki PAN przyjmuje Dział Wydawnictw IPPT.

Bieżące numery Engineering Transactions można nabyć bezpośrednio w Redakcji:
ul. Pawińskiego 5B, 02-106 Warszawa
Tel.: (48-22) 826 60 22; Fax: (48-22) 826 98 15
e-mail: subscribe@ippt.pan.pl

Arkuszy wydawniczych 6.25; Arkuszy drukarskich 5.00
Papier offset. kl. III 80 g.
Skład w systemie LaTeX K. Jezierska

ENGINEERING TRANSACTIONS • *Engng. Trans.* • **61**, 2, 87–98, 2013
Polish Academy of Sciences • Institute of Fundamental Technological Research (IPPT PAN)
National Engineering School of Metz (ENIM)

Mechanical Characterization of Pre-Fatigued Free-Cutting Steels under Dynamic Tension

Masaaki ITABASHI, Heikichi KOSEKI

Tokyo University of Science, Suwa
Department of Mechanical Systems Engineering
5000-1, Toyohira, Chino, Nagano 391-0292, Japan
itabashi@rs.suwa.tus.ac.jp

In the near future, toxic Pb will be prohibited to add to free-cutting steels. So far, many types of free-cutting steels without Pb have appeared. In order to compare dynamic mechanical properties of Pb added SUM24L steel (refer to JIS G 4804:2008, equivalent to AISI 12L14 steel) with those for Pb free SUM23 (equivalent to AISI 1215), high velocity tensile tests are carried out at a strain rate of 1×10^3 s^{-1}, at room temperature. A half of the specimens are pre-fatigued before the dynamic tensile test. This loading combination, fatigue and impact, simulates a certain service condition, normal operational loadings and an accidental dynamic loading. Tensile strength of the pre-fatigued specimens is less than that of the virgin specimens, to some extent, for both steels. Where the degradation is of almost the same level, replacement of the Pb added free-cutting steel with the Pb free steel may be possible.

Key words: dynamic tension, pre-fatigue, Pb free, free-cutting steel, degradation.

1. Introduction

The loading combination of fatigue-impact is one of the more under-developed engineering fields. Some pioneer works exist and are as follows. MacGregor and Grossman [1] found that for SAE1020 steel the ductile-brittle transition temperature of their cylindrical specimens with a circular notch tended to increase after rotary bending fatigue. Nakanishi and Haze [2] carried out Charpy impact tests for a normalized low carbon steel with pre-fatigue by pulsating tension. They also reported the increase of the transition temperature by pre-fatigue. With Vickers hardness test, Sato, Imamura and Kawarai [3] tried to detect such an increase of the transition temperature with low-to-medium cycle pre-fatigue conditions for a rolled steel structure. Thus, these pioneering works focused on the variation of the ductile-brittle transition temperature.

From the structural designers' viewpoint, the remaining dynamic strength and toughness of the materials of interest are also needed for members and structure with good durability against fatigue-impact loading.

Recently, the loading axes of pre-fatigue and succeeding tensile impact coincided with each other in order to simulate the service condition of investigated materials more accurately with a high velocity tensile testing technique. For three Al alloys damaged by low-cycle pre-fatigue in sinusoidal pulsating tension, deterioration of dynamic tensile strength and elongation was reported by KAWATA, ITABASHI and KUSAKA [4]. AUZANNEAU [5] found that on the side surface of pre-fatigued and dynamically-tensile-fractured 2017-T3 Al alloy specimen, there existed opened cracks of large lengths, typically 400 μm. According to his experimental results, ITABASHI, NAKAJIMA and FUKUDA [6] observed the side surface of pre-fatigued and dynamically-fractured 6061-T6 and 2219-T87 Al alloys with a scanning electron microscope and found that the number of relatively large cracks was one of the indicators of the loading combination type with some screening techniques.

On the other hand, for steels, such a deterioration of mechanical properties was not found. ITABASHI and FUKUDA [7] found this fact for two steels for building structure. TSUDA, DAIMARUYA, KOBAYASHI and SUNAYAMA [8] also confirmed that even automotive sheet steels did not reveal such a deterioration with the fatigue-impact loading combination. They carried out to investigate that fact not only for low-cycle pre-fatigue, but also for high-cycle pre-fatigue. Therefore, these steels are stronger to the fatigue-impact loading in tension than the Al alloys.

For free-cutting steels, their mechanical properties are functionally degraded, especially the local toughness. The second phase exists in steel matrix, as a chip breaker, tool edge stabilizer, and tool life extender. For these purposes, the second phase plays the role of a solid lubricant. Typical materials as the second phase in free-cutting steels are Pb and MnS. The existence of the second phase can be recognized as the stress concentrated point in the steels. Under the fatigue-impact combination, a relatively larger deterioration of the mechanical properties of free-cutting steels should appear than that for general structural steels.

In this paper, to clarify the above-mentioned theme, two free-cutting steels, a Pb added steel and a Pb free one, are pre-fatigued by low-cycle pulsating tension and tested quasi-statically and dynamically in tension. It is needless to say that Pb is prohibited to be alloyed in steel by more than 0.35% mass, by the RoHS (restriction of hazardous substances) directive. In the near future, this allowable range will be disappeared. Comparing experimental results of the steels, the possibility of replacing the former steel with the latter can be argued from such a loading combination aspect.

2. Experimental procedure

2.1. *Investigated free cutting steels*

The Pb added free-cutting steel is SUM24L steel (JIS G 4804:2008, equivalent to AISI 12L14 steel). The capital letter "L" in the above symbols means lead. The Pb free steel is SUM23 steel (equivalent to AISI 1215 steel). The chemical composition of the steels are tabulated in Table 1. In JIS G 4804:2008, the mechanical properties of the free-cutting steels are not prescribed. The manufacturing process of both steels was the same and was as follows. Each steel was melted in a factory converter, cast continuously and rolled into a square bullet of 155 × 155 mm. The bullet was cut into an appropriate length, heated at 1250°C for 30 min, hot forged into a ⌀12 mm cylindrical bar and cooled in air. The hot-forging process was important to distribute grains of Pb and MnS uniformly and to adjust the grain size. This process is the same as commercially available SUM24L and SUM23 steels.

Table 1. Chemical composition for the free-cutting steels investigated here (unit: % mass).

Material	C	Mn	P	S	Cr	Pb	Fe
SUM24L	0.08	1.12	0.084	0.297	0.04	0.24	Bal.
SUM23	0.08	1.00	0.085	0.322	0.03	–	Bal.

The steels were supplied in ⌀12 mm cylindrical bars. The bars were machined to the specimen configuration as shown in Fig. 1. After turning, the parallel part with round fillets of the specimen was ground by #4000 emery paper.

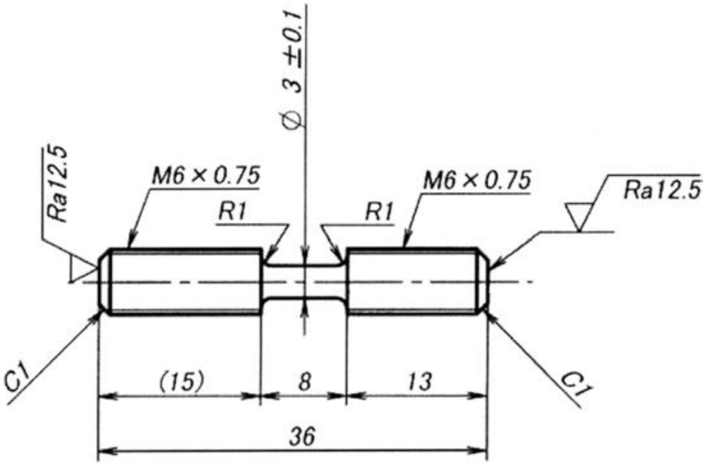

Fig. 1. Specimen configuration (in mm).

2.2. *Quasi-static tensile test*

At a strain rate of 1×10^{-3} s^{-1}, quasi-static tensile tests were carried out with a servohydraulic fatigue testing machine (Shimadzu Corp., Servopulser EHF-FB1 type 1111, crosshead speed: 0.5 mm/min). To improve the accuracy of the elongation measurement, specially designed specimen attachments were introduced with two clip gauges (Tokyo Sokki Kenkyujo Co., Ltd., UB-5L, gauge length: 5 mm), as shown in Fig. 2.

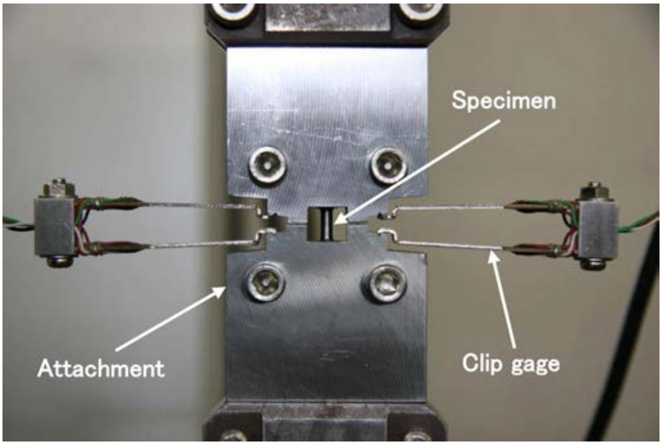

FIG. 2. Detail of the specially designed specimen attachments with two clip gauges for quasi-static tensile test.

At the beginning of this series of experiments, three quasi-static tensile tests for virgin (not pre-fatigued) specimens of each steel were executed. According to the quasi-static tensile strengths, fatigue test conditions were set appropriately.

2.3. *Fatigue test and pre-fatigue conditions*

For both steels, *S*-*N* curves were obtained, respectively. The curves were evaluated under sinusoidal pulsating tension (stress ratio: 0, frequency: 20 Hz) by the servohydraulic fatigue testing machine. Circular plots in Fig. 3 are the results of the fatigue tests. Bold solid lines are linear fitted lines obtained by the least square method.

Complying with the conditions of Al alloys [4, 6], pre-fatigue conditions were decided as follows. Maximum (pre-fatigue) stresses were set at 78 and 89% of the quasi-static lower yield strength, as shown in Fig. 3, i.e., 343 and 392 MPa for SUM24L steel, and 319 and 364 MPa for SUM23. Square and rhombic plots indicate (pre-fatigue) cycle ratios, 5 and 20% of the number of cycles to failure respectively. These severe conditions were the onset of the tensile strength degradation for the formerly investigated Al alloys [4, 6].

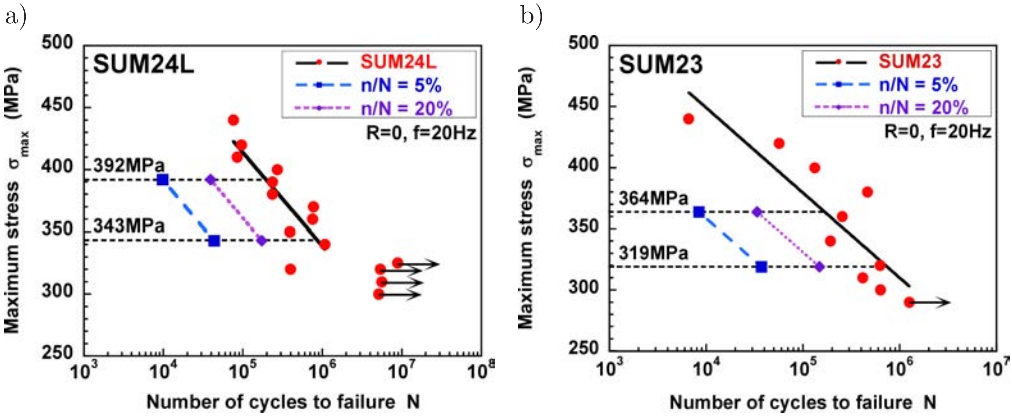

FIG. 3. *S-N* curves and pre-fatigue conditions: a) SUM24L steel, b) SUM23 steel.

2.4. Preparation of pre-fatigued specimens

With the servohydraulic fatigue testing machine, five pre-fatigued specimens were prepared for each pre-fatigue condition. Several specimens for SUM24L steel were fractured during the pre-fatigue. For SUM23 steel, no specimen was fractured during preparation.

2.5. Dynamic tensile test

Tensile tests at a dynamic strain rate of approximately 1×10^3 s^{-1}, were carried out with a high velocity tensile testing machine of a horizontal slingshot type [9]. This machine adopted the one bar method [10] to obtain dynamic stress-strain curves without ringing.

The principle of the one bar method is shown in Fig. 4. It consists of three elements, an impact block as a rigid body, a specimen, and an output bar as an elastic bar. Deriving from the one-dimensional elastic wave propagation theory and Hooke's law, the fundamental formulae for dynamic stress $\sigma(t)$, dynamic strain $\varepsilon(t)$ and strain rate $\dot{\varepsilon}(t)$ in nominal are as follows:

$$\sigma(t) = \frac{S_0}{S} E_0 \varepsilon_g \left(t + \frac{a}{c}\right), \tag{2.1}$$

$$\varepsilon(t) = \frac{1}{\ell} \int_0^t \left\{V(\tau) - c\varepsilon_g \left(\tau + \frac{a}{c}\right)\right\} d\tau, \tag{2.2}$$

$$\dot{\varepsilon}(t) = \frac{1}{\ell} \left\{V(t) - c\varepsilon_g \left(t + \frac{a}{c}\right)\right\}, \tag{2.3}$$

where t is the time after impact, ℓ and S are the gauge length and cross-sectional area of the specimen, S_0, E_0 and c are the cross-sectional area, Young's modulus,

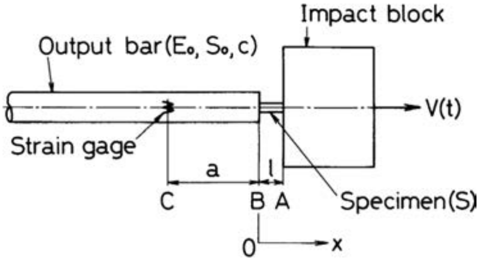

FIG. 4. Principle of the one bar method.

and longitudinal elastic wave velocity of the output bar, $V(t)$ is the velocity of the impact block, and $\varepsilon_g(t)$ is the strain of the output bar at the distance a from the loaded end.

The tensile impact load was generated by the horizontal slingshot machine. A hammer made of carbon steel, 50 kg in mass, can be accelerated to the velocity of 5–6 m/s. The accelerated hammer impinged on the impact block made of chromium molybdenum steel. The impact block of 0.7 kg in mass and $20(\mathrm{H}) \times 60(\mathrm{L}) \times 75(\mathrm{W})$ mm^3 in size, flew at the higher velocity, typically 7–8 m/s, than that of the hammer. Therefore, the maximum nominal strain rate attained 0.7×10^3–0.8×10^3 s^{-1} with the specimen of an initial gauge length of 8 mm.

Figure 5 shows a block diagram of the dynamic data acquisition system. In order to detect $\varepsilon_g(t)$, four semiconductor strain gauges (Kyowa Electronic Instruments, KSP-2-120-E3, gauge length: 2 mm, gauge factor: 120) were cemented onto the output bar made of type 304 stainless steel, at the location of 50 mm ($= a$) apart from the specimen-mounted end. The output bar was 3 m in length and ∅10 mm in diameter. The displacement of the impact block,

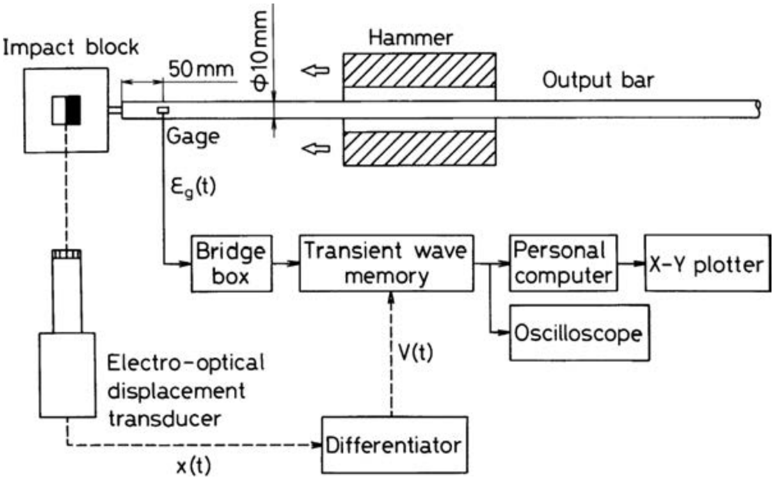

FIG. 5. Block diagram of dynamic data acquisition system for tensile stress-strain relation.

$x(t)$ was detected by an electro-optical displacement transducer (Zimmer Model 100D/II, gauge length of an installed lens: 10 mm). This signal was differentiated with respect to time by a differentiator (Zimmer Model 131C) in order to obtain the velocity of the block, $V(t)$. The output bar strain $\varepsilon_g(t)$ and impact block velocity $V(t)$ were stored in two synchronized digital memories (Kawasaki Electronica, TMR-100, sampling frequency: 1 MHz, resolution: 10 bits, memory length: 4 kwords).

3. Results and discussion

3.1. *Obtained stress-strain curves*

The tensile stress-strain curves for the virgin specimens up to fracture are shown in Fig. 6 and for the pre-fatigued specimens in Fig. 7. The stress-strain

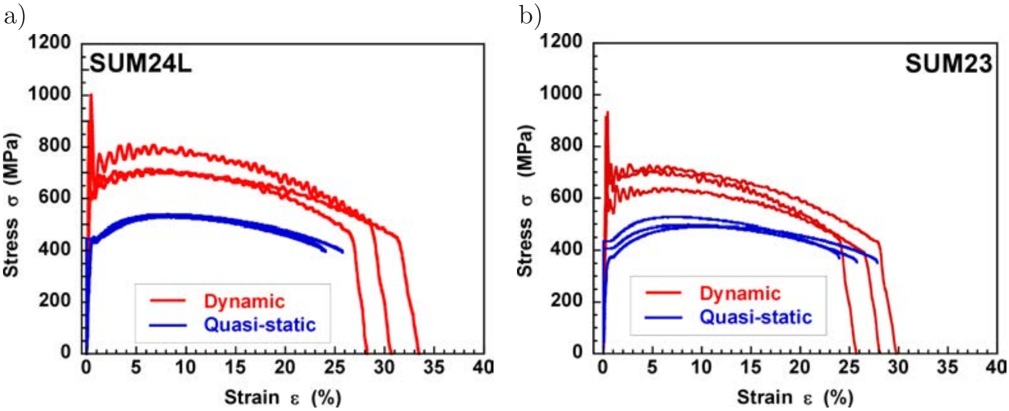
a) b)

Fig. 6. Tensile stress-strain curves for virgin specimens: a) SUM24L steel, b) SUM23 steel.

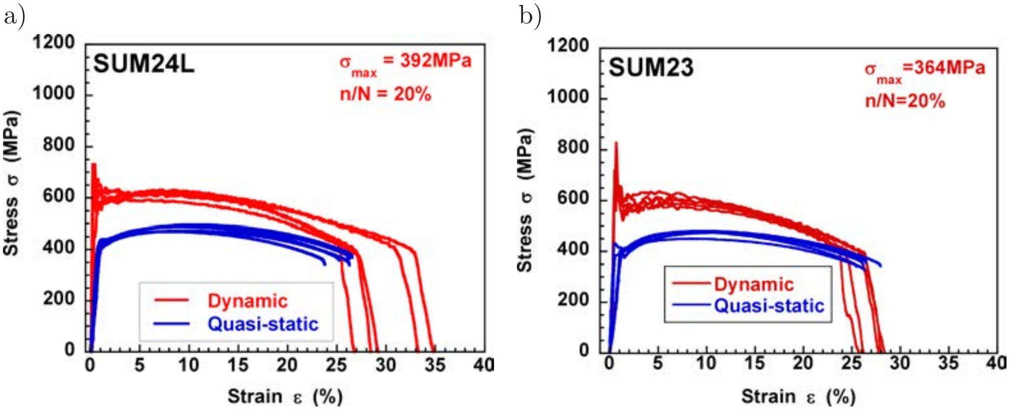
a) b)

Fig. 7. Tensile stress-strain curves for pre-fatigued specimens ($\sigma_{\max} = 392$ MPa for SUM24L steel and 364 MPa for SUM23 steel, $n/N = 20\%$): a) SUM24L steel, b) SUM23 steel.

curves for both steels shown in Fig. 6 are standards of a succeeding series of the present experiments. Generally speaking, the virgin curves are higher than the pre-fatigued curves. The pre-fatigue condition in Fig. 7 is the severest one for each steel; thus there is an obvious deterioration of flow stress, but it is not so much, typically 100–150 MPa.

3.2. *Remaining strength*

The fatigue cycle ratio dependence of the deterioration of the remaining (tensile) strength is shown in Figs. 8 and 9. Taking fatigue cycle ratio as an abscissa, the results of the virgin specimen correspond to plots of $n/N = 0\%$. The number of plots of $n/N = 0$ is three, and those of $n/N = 5\%$ and 20% are

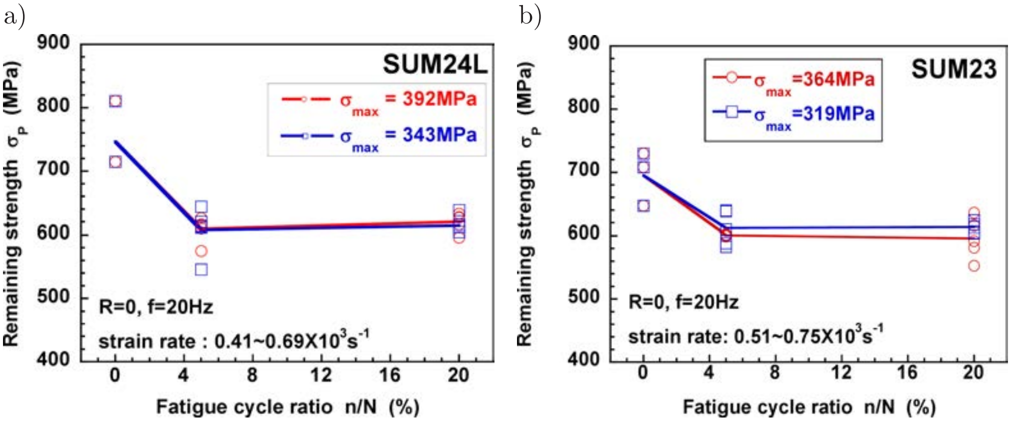

FIG. 8. Fatigue cycle ratio dependence of dynamic tensile strength for free-cutting steels: a) SUM24L steel, b) SUM23 steel.

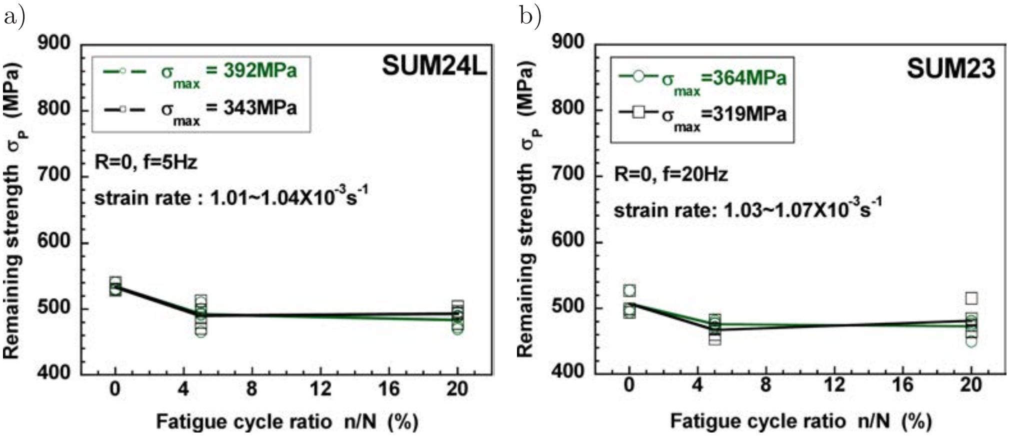

FIG. 9. Fatigue cycle ratio dependence of quasi-static tensile strength for free-cutting steels: a) SUM24L steel, b) SUM23 steel.

five for each maximum (pre-fatigue) stress. In Fig. 8, even with the virgin condition, plots are widely scattered. The cause of this scatter may be the relatively small specimen diameter, since grains of the second phase were not so uniformly distributed in the gauge length of the specimen. Beyond the scattering width, the remaining dynamic strength in Fig. 8 deteriorates at a ratio of 5% for both steels. But, this lowered strength is maintained at 20%. From the viewpoint of well-known damage mechanics, this tendency is unusual. In such a case, the remaining strength will decrease monotonously with increasing cycle ratio. On the contrary, for these free-cutting steels, it does not seem unusual that the steel matrix around the second phase can be hardened by stress concentration. Therefore, between the ratio of 5% and 20%, it is possible to explain that some weakening of the total strength by pre-fatigue is balanced with some hardening of the local stress concentration. In Fig. 9, the deterioration of quasi-static remaining strength is smaller than that of dynamic one. The quasi-static strength for both steels keeps the constant level between the fatigue cycle ratio of 5% and 20% too.

The deterioration of the remaining strengths at both strain rates does not depend on maximum (pre-fatigue) stresses. This suggests that the second phase, Pb and MnS have been debonded from the matrix due to the weak strength of the second phase itself during pre-fatigue. This hypothesis can be confirmed by lowering the maximum (pre-fatigue) stress level to the tensile strength of Pb, typically 10 MPa. Then, such deterioration at the fatigue cycle ratio of 5% will be reduced.

3.3. Breaking strain

The breaking strain in a dynamic tensile test tends to scatter. The distributed second phase in free-cutting steels is one of the main factors of fracture. Dynamic breaking strain of the free-cutting steels is widely scattered, as shown in Fig. 10. In general, the pre-fatigue decreases the breaking strain, except for the condition of $\sigma_{\max} = 364$ MPa and $n/N = 5\%$. It can be thought that Pb and MnS were not so uniformly distributed even after the hot-forging process. On the other hand, quasi-static breaking strain gives the opposite tendency, as shown in Fig. 11. In the second phase, Pb and MnS may be the cause of these different tendencies. At the quasi-static strain rate, the soft second phase helps necking growth, easily deforming from the original shape in the hard matrix.

This scattering of these breaking strains may be reduced by utilizing larger specimens, for example, $\varnothing 10$ mm in diameter. This value is comparable to a standardized quasi-static tensile specimen. According to the capacity of dynamic tensile testing machine, the diameter of the parallel part of the present specimen is only $\varnothing 3$ mm.

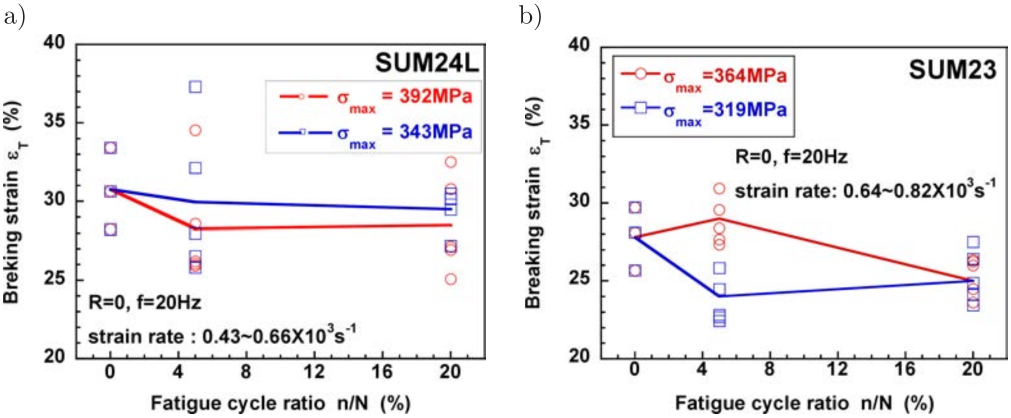

FIG. 10. Fatigue cycle ratio dependence of dynamic breaking strain for free-cutting steels: a) SUM24L steel, b) SUM23 steel.

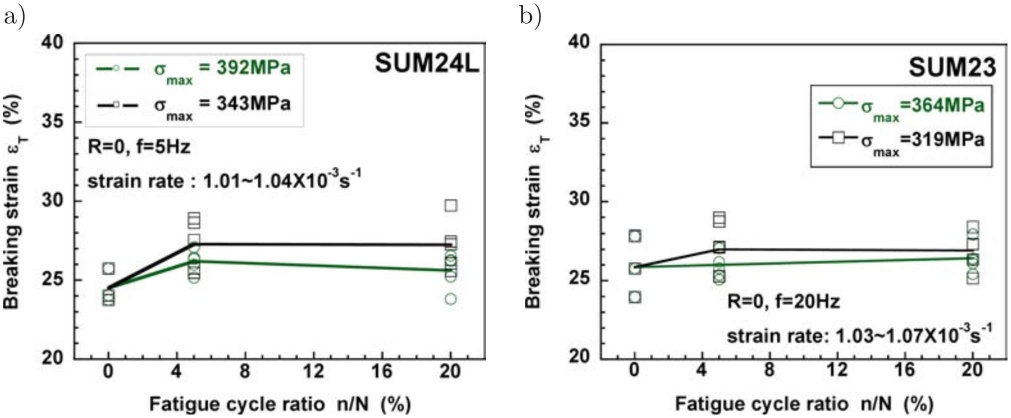

FIG. 11. Fatigue cycle ratio dependence of quasi-static breaking strain for free-cutting steels: a) SUM24L steel, b) SUM23 steel.

3.4. Absorbed energy per unit volume

The dynamic absorbed energy per unit volume is an important factor of impact resistance. Figure 12 shows the deterioration of dynamic absorbed energy. For SUM23 steel at $n/N = 5\%$, the dynamic absorbed energy of $\sigma_{\max} = 364$ MPa is larger than 319 MPa. No rational explanation can be given for this tendency; however, this tendency reflects the dynamic breaking strain tendency of Fig. 10b. Quasi-static absorbed energy is relatively stable, as shown in Fig. 13. The deterioration of strength is recovered by the slight increase of breaking strain.

From the obtained results, the pre-fatigue affects the impact tensile resistance of the free-cutting steels intensely. However, the dynamic strengths and absorbed energies are always higher than the quasi-static ones. Thus, the strain rate effect on the absorbed energy per unit volume is superior to the pre-fatigue effect.

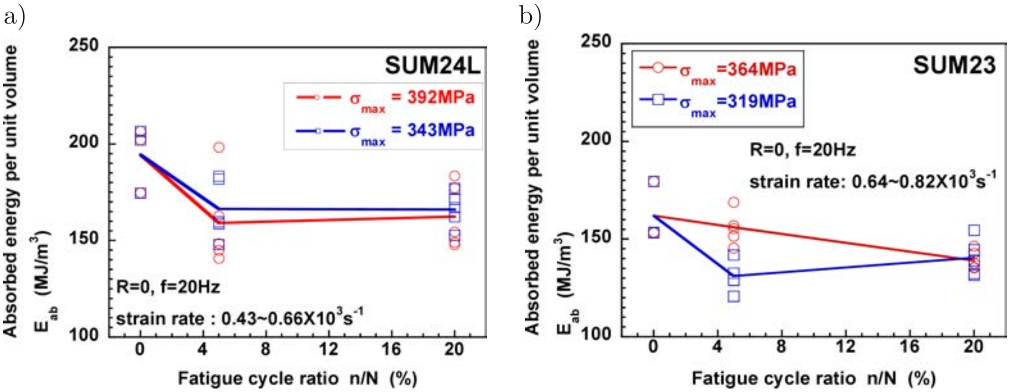

FIG. 12. Fatigue cycle ratio dependence of dynamic absorbed energy per unit volume for free-cutting steels: a) SUM24L steel, b) SUM23 steel.

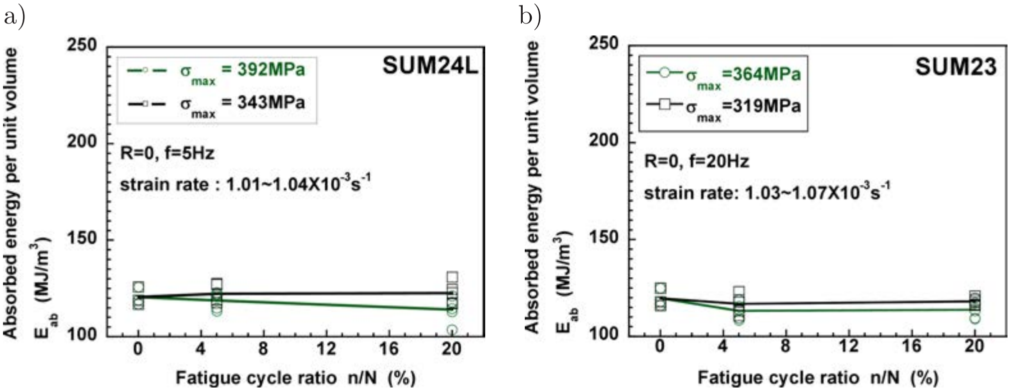

FIG. 13. Fatigue cycle ratio dependence of quasi-static absorbed energy per unit volume for free-cutting steels: a) SUM24L steel, b) SUM23 steel.

4. CONCLUSIONS

A Pb added free-cutting steel, SUM24L (equivalent to AISI 12L14) steel, and a Pb free free-cutting steel, SUM23 (AISI 1215) steel, were investigated to confirm the tensile impact resistance with the severe pre-fatigue conditions. Generally speaking, the pre-fatigue has a negative effect on the strength of free-cutting steels, at not only the quasi-static strain rate of 1×10^{-3} s^{-1}, but also the dynamic strain rate of 1×10^{3} s^{-1}. Regardless of the strain rate, the pre-fatigue process makes the scatter of mechanical properties wider. The weakened bonding and debonding between the matrix and second phase may be one of the main causes of the scatter and deteriorated mechanical properties. From the dynamic tensile stress-strain curves for both steels, 20%-reductions in strength and absorbed energy are observed respectively. From the quasi-static curves, 10%-reductions in strength and absorbed energy are obtained. Both steels reveal that they have almost the same mechanical properties and the same tendencies to the present fatigue-impact loading combination. Thus, SUM24L steel can be replaced with SUM23 in this particular simulation.

This article discusses only phenomenological aspects. However, such degradation of these mechanical properties for the investigated free-cutting steels has not been published as far as the authors know. In the near future, the mechanical damage of the interface between the steel matrix and second phase will be observed microscopically, and the affect of the interface on the observed pre-fatigue effect will be investigated and reported.

References

1. MacGregor C.W., Grossman N., *Some New Aspects of the Fatigue of Metals Brought out by Brittle Transition Temperature Tests*, The Welding Journal, Welding Research Supplement, **27**, 132-s-143-s, 1948.
2. Nakanishi S., Haze T., *The Change of Impact Characteristics under the Repeating Load* [in Japanese], Tetsu-to-Hagane, **52**, 4, 654–656, 1966.
3. Sato S., Imamura Y., Kawarai, T., *Determination of Increase in Brittle Transition Temperature of Steel Due to Fatigue by Hardness Test* [in Japanese], Journal of the Society of Materials Science, **25**, 270, 290–295, 1976.
4. Kawata K., Itabashi M., Kusaka S., *Behaviour Analysis of Pre-Fatigue Damaged Aluminum Alloys under High-Velocity and Quasi-Static Tension*, [in:] IUTAM Symposium on Micromechanics of Plasticity and Damage of Multiphase Materials, Pineau A., Zaoui A. [Eds.], Kluwer Academic Publishers, Dordrecht, 397–404, 1996.
5. Auzanneau T., Influence d'un Pré-Endommagement par Fatigue sur la Tenue an Choc – *Application à un Alliage d'Aluminium 2017A T3* [in French], PhD Thesis, Ecole Nationale Supérieure d'Arts et Métiers, Bordeaux, France, 1999.
6. Itabashi M., Nakajima S., Fukuda, H., *Microscopic Observation of the Side Surface of Dynamically-Tensile-Fractured 6061-T6 and 2219-T87 Aluminum Alloys with Pre-Fatigue*, JSME International Journal, Ser. A, **48**, 4, 222–227, 2005.
7. Itabashi M., Fukuda H., *High Velocity Tensile Mechanical Behavior for Low-Cycle Pre-Fatigued SN490B Steel (Rolled Steel for Building Structure)* [in Japanese], Journal of the Society of Materials Science, Japan, **53**, 3, 260–265, 2004.
8. Tsuda H., Daimaruya M., Kobayashi H., Sunayama Y., *Effect of Pre-Fatigue on Impact Tensile Properties of Laser Welded Butt Joint of High Strength Steel Plates* [in Japanese], Journal of the Society of Materials Science, Japan, **55**, 9, 824–830, 2006.
9. Itabashi M., Kawata K., *Carbon Content Effect on High-Strain-Rate Tensile Properties for Carbon Steels*, International Journal of Impact Engineering, **24**, 2, 117–131, 2000.
10. Kawata K., Hashimoto S., Kurokawa K., Kanayama N., *A New Testing Method for the Characterization of Materials in High Velocity Tension*, [in:] *Mechanical Properties at High Rates of Strain 1979, Institute of Physics Conference Series No. 47*, Harding J. [Ed.], Institute of Physics, Bristol and London, 71–80, 1979.

Received December 20, 2010; revised version January 31, 2013.

ENGINEERING TRANSACTIONS • *Engng. Trans.* • **61**, 2, 99–117, 2013
Polish Academy of Sciences • Institute of Fundamental Technological Research (IPPT PAN)
National Engineering School of Metz (ENIM)

Failure Analysis (Experimental and Numerical Approach) of Gas Turbine Generator Cooling Fan in Comparison between using 2types (14° and 19° Angle of Attack) of Blades

Ali JAHANGIRI[1], Seyed Ebrahim Moussavi TORSHIZI[2],
Seyed Majid Yadavar NIKRAVESH[3]

[1] *Semnan University, Faculty of Mechanical Engineering*
Semnan, Iran
e-mail: a_jahangiri@sun.semnan.ac.ir

[2] *NRI – Niroo Research Institute*
P.O. Box 14665/517, Tehran, Iran
e-mail: emoussavi@nri.ac.ir

[3] *Power & Water University of Technology*
P.O. Box 16765-1719, Tehran, Iran
e-mail: nikravesh@pwut.ac.ir

In gas turbine power plants, a fan is used as a cooling system to dissipate generated heat in coils (copper conductors) and generator electric circuits at the end sides of its rotor. In some cases, fracture of blades causes a short circuit between rotor and stator and consequently generator explosion and financial problems. The fracture of cooling fan blades has occurred five times at the turbine side of the generator in our case of study, just 100hr after resuming operations after an overhaul.

Using numerical analysis as well as laboratory investigation – including visual inspections, metallography and SEM – can help better find failure problems that cause blade failures. A series of numerical analysis was performed to diagnose the possible cause of failure. CFD analysis is used to study the airflow distribution in order to observe probable separation phenomenon and pressure forces as they are imposed on fan blades due to operation. A finite element method was utilized to determine the stresses and dynamic characteristics of the fan blade (natural frequencies, stresses and vibrations).

Key words: fatigue failure, dimple rupture, fan blade, scanning electron microscope (SEM), resonance, fan blade angle of attack, computational fluid dynamic (CFD), finite elements.

1. Introduction

There are eleven blades on both sides of generator, which have been installed and are separated with eleven spacer pieces. Figure 1 shows the position and

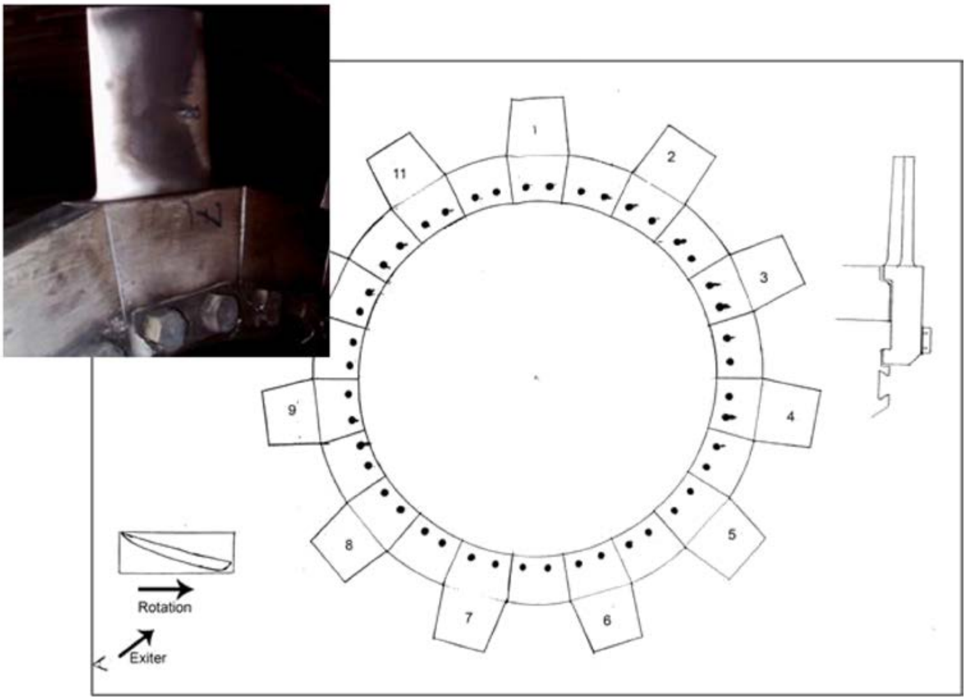

FIG. 1. Setting of blades with their spacers around a retaining ring [1, 5].

arrangement of blades and spacer pieces on a retaining ring. The axial fan has been utilized as a cooling system manufactured by GEC-ALSTHOM Belford under the following conditions; Turbine rotation = 3000 rpm; output power = 118 MW [9, 11, 12].

It must be noticed that all of the fractured blades have a 19°-angle of attack and after failure GEC-ALSTHOM replaced them by 14°-angle of attack (without a change in alloy type) in order to decrease the forces applied to the blades. The width of the 14°-blades is lower than the 19°-blades, but their length is the same. Both type of blades are compared in Fig. 2 which also defines the differences between angle and blade dimensions.

In accordance with previous studies of failure, some examples are listed below: Xi *et al.* [13] investigated the failure of disk and blade for the first stage of the compressor in an aero engine. Metallurgical analysis and investigation of stress clarified that the design was not accurate, which resulted from extreme load of centrifugal bending moments and improper contact conditions.

Beisheim and Sinclair [4] and Hou *et al.* [6] performed a series of mechanical analyses and examination of a damaged blade in a gas turbine engine and utilized nonlinear finite elements to determine the stress of the blade in order to identify the cause of blade failure.

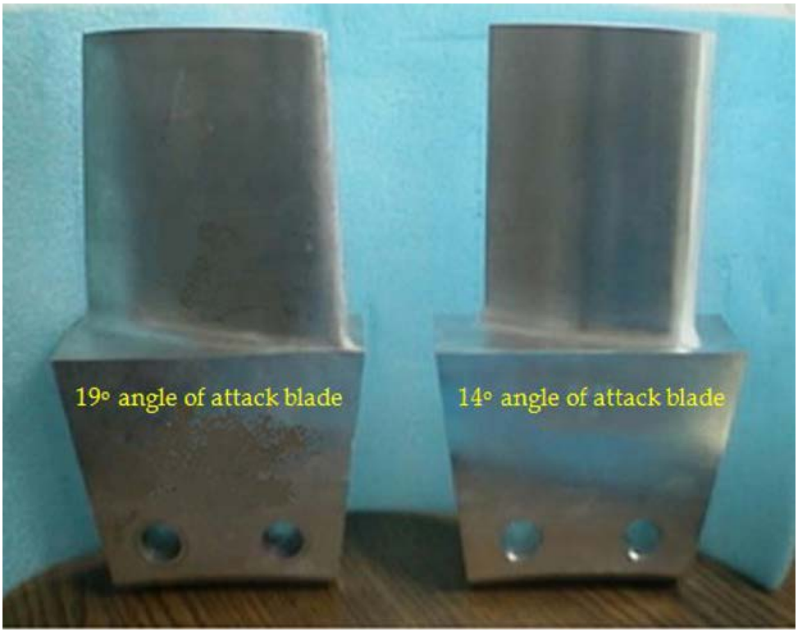

Fig. 2. Dimensional deference between 2 types of blade [5].

Hutson *et al.* [7] verified the efficiency of a method of fracture mechanics used to model the crack growth behavior of fatigue nucleated cracks obtained under tested conditions similar to those found in turbine engine blade attachments and the calculated Crack propagation lives using stress results of FEM analysis. Barlow and Chandra [3] simulated the three dimensional fatigue crack in a typical military aircraft engine fan blade attachment by Franc3D.

In the remainder of this paper, two series of analysis (laboratory investigation and Numerical) have been performed, and their results are evaluated to identify the possible causes of failure.

To study the reasons for blade fracture, this matter was reviewed and studied from different points of view as in the following (laboratory investigation):

1. Review of the history of blade repairs and/or modifications (change in blade angle of attack from 19° to 14°).
2. Material and microstructure (quantometry).
3. Metallurgical examination of fractures to identify the metallurgical mode of failure (SEM).

In the first part, studies on ruptured surfaces have shown that fracture would occur as a result of high cycle fatigue (hcf) [6]. The presented numerical research will prove this result and show that the probability of failure can be weak by changing the angle of attack from 19° to 14°.

The numerical investigations are listed below:

1. CFD analysis in order to study the imposed stresses of the fan blades due to operation.
2. Application of the finite element method for modal and harmonic analysis to compute the natural frequencies, stresses and vibration.

2. Mechanical and laboratory investigation

2.1. Visual inspection

The statistical data revealed that all of these failures happened at the first hours of operation after gas turbine repair, this means that no fracture has happened after 100 hr of operation. On opening the turbine casing, three kinds of blades (for using a 19°-attack angle) were found: A broken one, a cracked one, and blades having no failure. The failure was at the turbine side of the generator and there was no crack on the exciter side. The failure occurred at the transition section (airfoil and blade root tangency). The crack initiation point was at the central part of the airfoil on its concave surface. Some parts of the surface appeared black and pitted due to an electric spark; but, by changing the attack angle of the blades to 14° no failures have been seen. However, temperature rise in the generator casing is higher than 19° and resulted from decreasing the sucked air flow rate for generator cooling [5].

2.2. Microstructure and metallurgical investigation

The quantometry test technique is used for chemical composition of blade material specification and this composition compared with some metal alloy composition that is available in reference books. It confirms that the composition of the blade material is similar to the aluminum 2024 alloy (Table 1). Also the result of a metallurgical examination over blades shows that the blades are not produced by die casting, but rather by molding, milling, and shaping, and finally the blades surfaces would be polished. Crystals, which have been formed in the

Table 1. Chemical composition of the blade and its comparison with aluminium 2024 alloy.

Elements	Al	Zn	Si	Fe	Mn	Mg	Cu
quantometry test	Base	0.07	0.07	0.11	0.67	1.36	3.97
Al 2024 [8]	Base	–	–	–	0.6	1.5	4.4
Al 2024 [11]	Base	Max 0.25	Max 0.5	Max 0.5	0.3–0.9	1.2–1.8	3.8–4.9

blade length direction, are a proof of this claim. Heat treatment performed in this blade is T351 heating operations [9]. Some important blade and material mechanical behavior are derived and presented in Tables 2 and 3.

Table 2. Mechanical strength of aluminium 2024 [8].

Alloy	Ultimate tensile stress [9] σ_{ut}	Yield tensile stress [9] σ_{yp}	Fatigue endurance limit σ_e
Al 2024	470 MPa	325 MPa	140 MPa
Al 2024 @ Temperature 24°C	469 MPa	324 MPa	140 MPa
Al 2024 @ Temperature 100°C	434 MPa	310 MPa	140 MPa

Table 3. Mechanical properties of aluminium 2024 [8].

Alloy	Poisson's ratio Υ	Elasticity modulus E			Density P	Coefficient of thermal expansion α	Melt Point
		Tension	Shear	Pressure			
Al 2024	0.33	72.4 GPa	28.0 GPa	73.8GPa	2770 Kg/m^3	22.9 μm/m·K	638°C

2.3. Study of fracture surfaces by SEM

Generally, blade failures can be sorted into two categories [2, 10]:

1. Gradual failure in the effect of endurance (fatigue).
2. Failure in result of external material impact (dimple rupture).

It is obvious that one of the most important ways of investigating the failure pieces, is to study the failure of surfaces. This section engages with the inspection of failure surfaces and defining its result.

In order to study the failure surface and compare the quality of these two possible failure mechanisms with a standard failure handbook of this alloy, to diagnose the main reason of failure, a Scanning Electron Microscope (SEM) was employed. SEM is used to prepare the best high quality picture of a surface with the highest accuracy (scaled to ×1000) for investigation of the microstructural difference between failure surface types.

In this investigation, the theory of fatigue failure and dimple rupture is considered. A 1×1 cm piece of blade alloy has been prepared and broken with a single external material impact; also, by using fractured surface of blade which has been broken in power plant, both types of fractured surface are compared with surfaces that have been shown in reference books. By comparison of Fig. 3 (the surface of a broken blade at a power plant incident) and Fig. 4 (broken in type

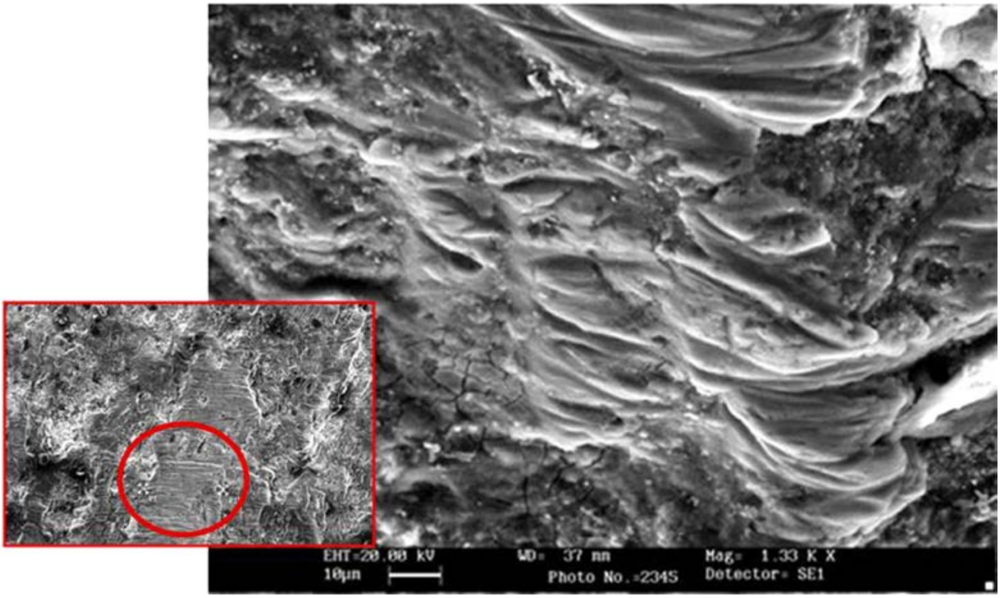

FIG. 3. Fatigue surface failure (scaled ×1330).

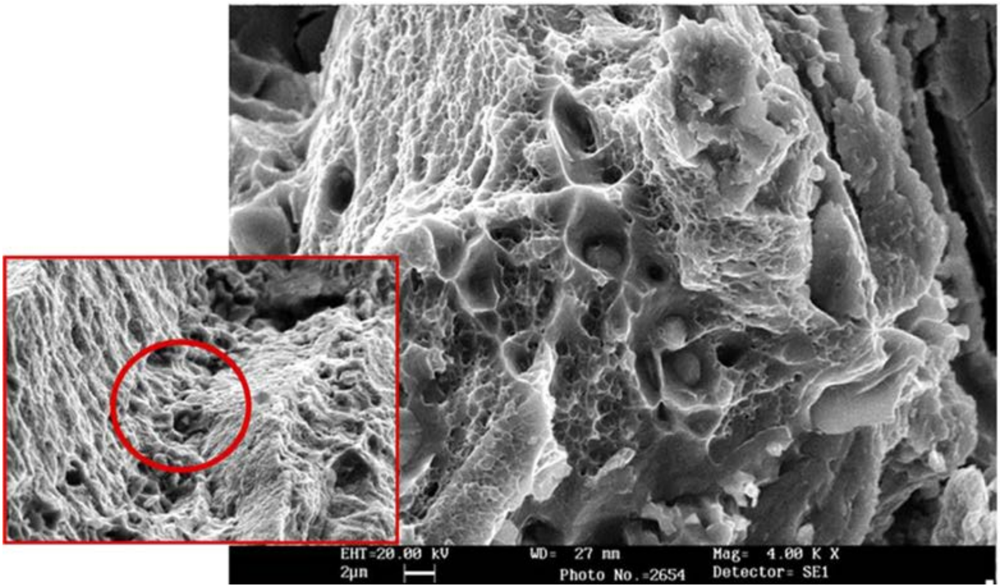

FIG. 4. Dimple rupture result of instant impact (scaled ×4000).

of dimple rupture (breaking potholes)) with reference books, it can be clearly observed that existing lines on Fig. 4 are fatigue lines. The fatigue lines show that the crack is initiated at one side and propagated with the passing of time.

Concerning a reference fatigue fracture surface, Fig. 5 shows that the final fracture occurs in accordance with crack propagation and results in periodically applied forces and fatigue.

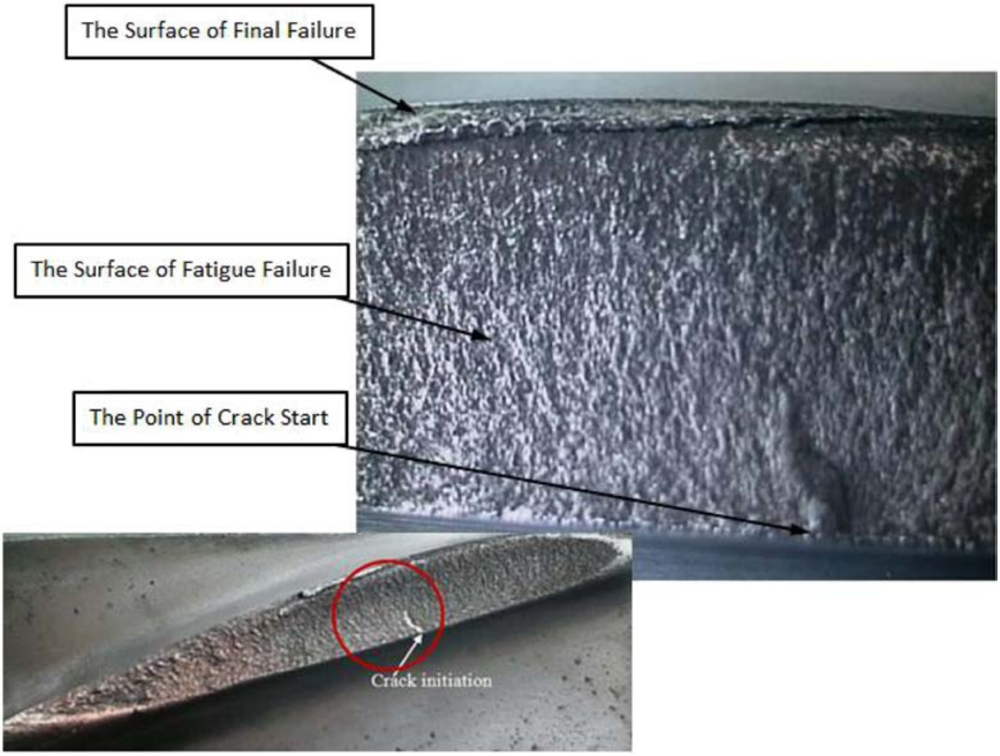

Fig. 5. Final and fatigue failure surface.

3. Numerical analysis on 14° and 19°-blades

Separation phenomenon and vortex flow are factors that may cause vibration in fan blades due to vortex flow creation, the pressure distribution (air flow forces) at two sides of fan blades change in an oscillatory way [9]. In order to study the aforementioned phenomenon, and also the distribution of air pressure forces on blade body due to operation, fan blades and their effective domain should be simulated. To do this, CFD (Computational Fluid Dynamic) code and FEM (Finite Element Method) were employed to analyze air flow distribution and vibration respectively.

Vibration due to the oscillatory change of pressure distribution may cause blade fatigue on two sides of blade [10]. Therefore the purpose of CFD analysis is to achieve an air velocity distribution around blades and also to study air flow patterns (in order to discern probable vortex forming) and also for the determination of the force resulting from air pressure over blades. In this order after determination of 14° and 19°-blade profile is prepared by using a scanning digitizer camera with higher than micron accuracy. Then, the air passage channel and related domain modeling is necessary, which was performed by CAD software as shown in Fig. 6 and the 3-dimentional model thus obtained, is then imported to mesh generation software, which generates the meshing for the volume as shown in Fig. 7.

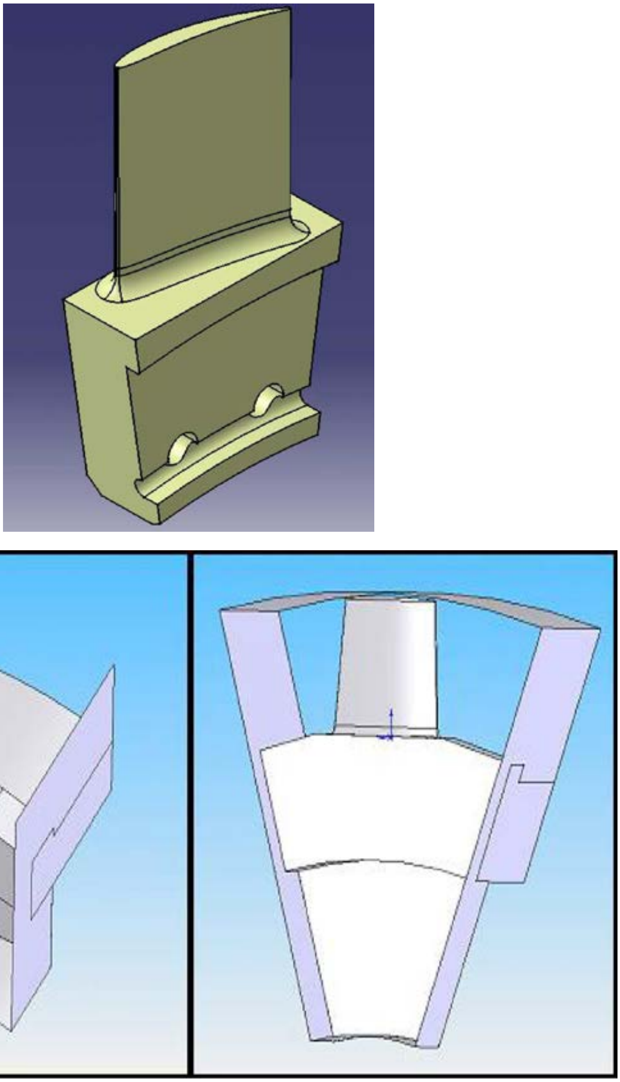

Fig. 6. 3-dimensional model of blade and related passage channel.

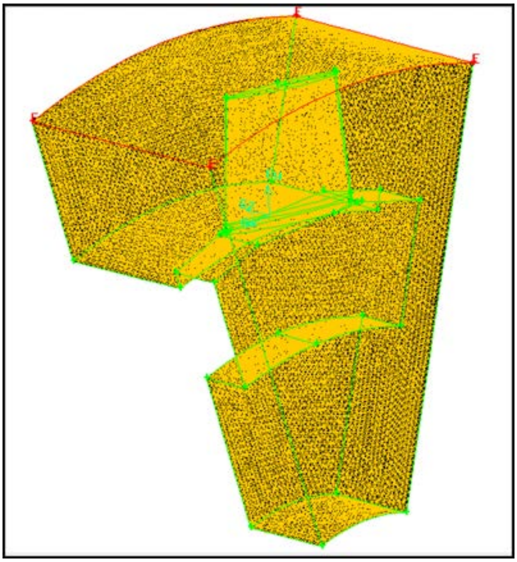

FIG. 7. Meshing domain in solution range.

3.1. *Computational fluid dynamics (CFD) analysis*

3.1.1. Solution procedure. Because of the turbulent action induced by high Reynolds swirling flow pattern, the standard k-ε two-equation turbulence model, the continuity and momentum are selected.

In these kinds of problems where a moving object is the cause of fluid flow, it is possible to take the rotational component of the axial velocity of air to count blade rotation (equivalent to 314.1592 rad/s as calculated: $\omega = 2\pi \times 3000$ R.P.M/60) [9, 12]. The total volumetric flow of the cooling air is 45.6 m^3/s using both type of blades, and half of that is directed towards fan at the turbine end and the other half is directed towards fan at the exciter end. At the inlet duct cross-section, the velocity of air is calculated as $V = (Q/2)/A = 16.71$ m/s (also, it should remain in mind that the area of air passage, is the difference between the channel, which is a circle with a radius of 69.6 cm, and generator shaft cross-section, which is a circle with a radius of 22.5 cm [8]). Air pressure is uniform for all of the outlet area and along its duct, which will be approximately equal to ambient pressure. For reduction of the solution domain to reach the least logical possible domain, a periodic analysis would be used.

3.1.2. Analysis of flow field and pressure. As seen in Fig. 8a and b, in both blade types the airflow pattern is typical. It is observed that the path lines are completely tangent over the blades and the separation phenomenon has not incurred.

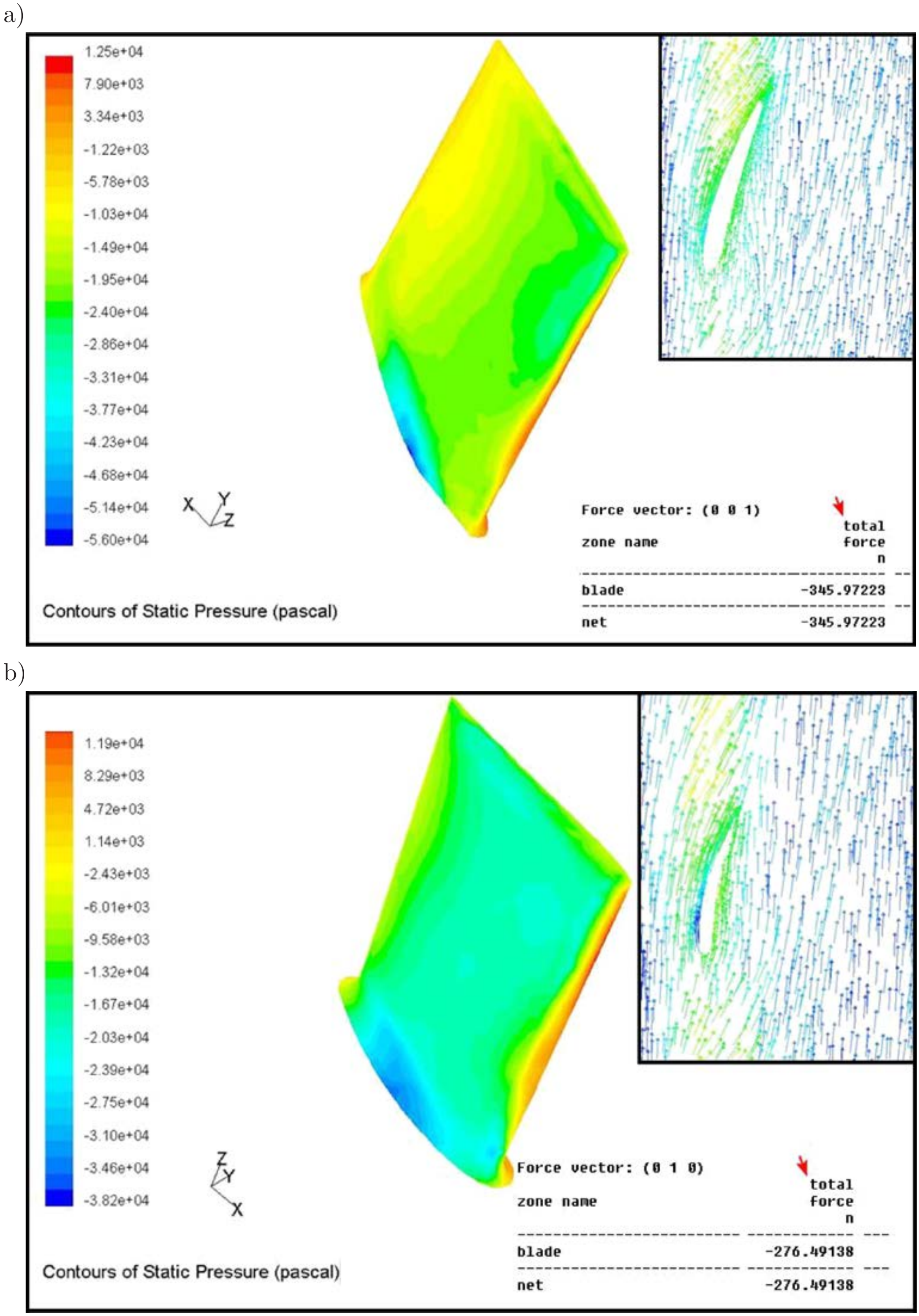

```
Force vector: (0 0 1)
                                   total
zone name                          force
                                       n
-------------------------------------------- --
blade                         -345.97223
-------------------------------------------- --
net                           -345.97223
```

```
Force vector: (0 1 0)
                                   total
zone name                          force
                                       n
------------------------- ------------ ---
blade                         -276.49138
------------------------- ------------ ---
net                           -276.49138
```

Fig. 8. a) Pressure contour and velocity vectors passed over 19°-angle of attack blade, and b) pressure contour and velocity vectors passed over 14°-angle of attack blade.

The air pressure distribution can also been seen over the blades in these two figures. The maximum absolute value of pressure that is imposed on the 19°-angle of attack blade reaches 56 kPa on the bottom of the blade surface and the resultant force over the blade is approximately equal to 346 N. The results of tension for the mentioned force, is less than the amount that solely causes breaking of the blade.

Also in the 14°-blade, the maximum pressure at the bottom of the blade reaches 39 kPa and is even less than for the 19°-blade.

While the 19°-angle of attack blade has been changed with a 14°-blade, the amount of force imposed on the blade would decrease nearly 20% and is reduced from 346 to 276 N, then, these forces caused by air flow are not enough to cause blade rupture.

3.2. Finite element method analysis (FEM)

In order to determine the applied stresses on the blade and investigate the possibility of its failure resulting from resonance, the finite element method was used. A 3D numerical model of a gas turbine generator cooling fan blade was constructed and meshed to get the FEM of a single blade. The FEM has a structured mesh with ninety twenty-node solid elements to employ structural analyses, which have compatible displacement shapes and are well suited to model curved boundaries due to the complexity of the geometry. This blade was analyzed under two followings categories of FEM analysis [4, 5]:

1. Modal analysis;
2. Harmonic analysis.

The modal analysis on natural frequency and the harmonic analysis was done based on different excitation frequencies.

3.2.1. Modal analysis. First, the amount of bolt tightening and clearance between the blade root and retaining ring were modeled as constraints and their affect on the first natural frequency of the blade was studied as shown in Table 4. To evaluate these conditions, four different constraints were investigated for both the 19° and 14°-blade:

1. Just points around the bolts are assumed to be fixed.
2. All points from the surface of blade's root to the bolts are assumed to be fixed.
3. The contact surface with the retaining ring, as well as points mentioned in item two, are assumed to be fixed
4. The whole part of blade's root are assumed to be fixed in all directions.

Table 4. Calculated natural frequency in the first mode for four-bolt tightening states.

Bolts tightening state number	First Natural Frequency (Hz) 19° blade	First Natural Frequency (Hz) 14° blade
State No 1	480.97	367
State No 2	489.58	375.3
State No 3	513	394.9
State No 4	537.88	413.49

Based on Table 4, the first natural frequency of the blade for the fourth assumed constraint in both type of blades is bigger than the others.

The natural frequency in the five modes for these four states were calculated. Table 5 shows the natural frequencies for the fourth constraint in both type of blades.

Table 5. Calculated natural frequency in the 5 modes for 19° and 14°-blade.

Mode shape number	Natural Frequency (Hz) 19° blade	Natural Frequency (Hz) 14° blade
Mode No 1	537.88	413.49
Mode No 2	1339.8	1232.6
Mode No 3	2693.8	2365.9
Mode No 4	2637.1	2794.5
Mode No 5	3879.5	3837.1

In Fig. 9 the displacement of the tip of both blades at the first modal shape has been represented with Finite Element modeling. With respect to the fact that the first natural frequency of the 19°-angle of attack blade in the fourth state (538 Hz) was very close (almost within a 2% relative difference) to the frequency of the exciting force caused by shaft rotation (11 blades × 50 rad/s = 550 Hz) and therefore the incurrence of resonance in the above conditions is very probable. This state has been selected for finite element harmonic numerical simulation. Whereas 19°-blades are replaced with 14°-blades such that the natural frequency in the fourth mode (413.49 Hz) will not be close (with 33% relative difference) to exciting frequency and therefore resonance conditions will not occur.

3.2.2. Harmonic analysis In harmonic analysis, the frequency of external forces (air flow and shaft rotating force) acting on the blades, gradually increases, (from zero to 1000 Hz) then, domain, difference shapes of vibrations and tension a)

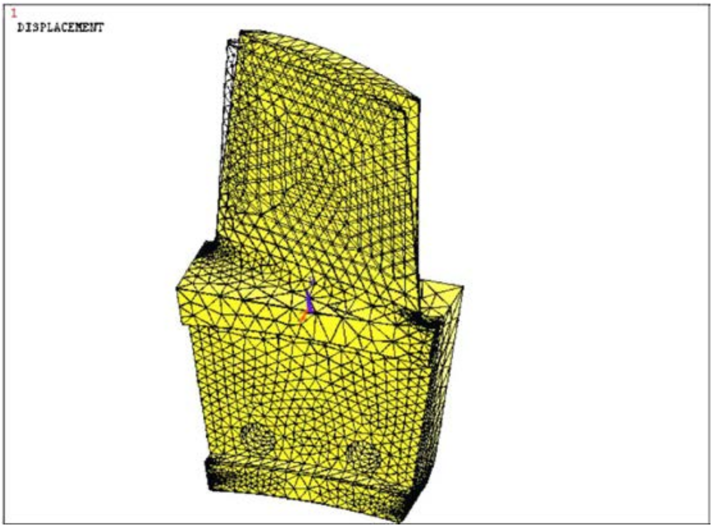

b)

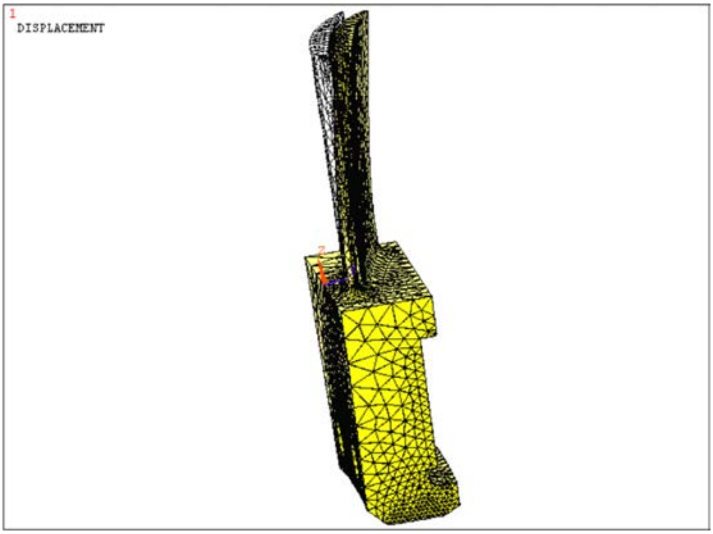

Fig. 9. a) Blade tip displacement at the first modal shape for a 19°-angle of attack blade, and b) blade-tip displacement at the first modal shape for a 14°-angle of attack blade.

result of these acting external forces with, changing in blade type, account for the various frequencies.

3.2.3. Harmonic analysis for 19°-blade. From CFD analysis force acted by air flow on 19°-blade was calculated about 346 N. By acting these external forces to blade in the various frequencies (between 0 to 1000 Hz), blade tip oscillation domain (blade tip displacement), is accounted with finite element analysis. The blade-tip displacement for these conditions is shown in Fig. 10.

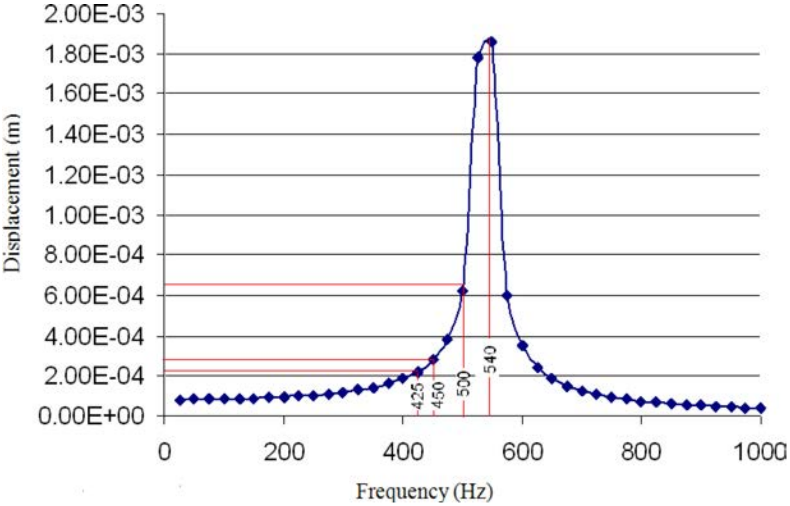

Fig. 10. 19°-blade-tip displacement at various frequencies in the first mode of vibration.

As seen, at a frequency of 50 Hz, the blade tip displacement reaches around 82 μm, and this value grows with increasing frequency up to the extent of 425 to 450 Hz and reaches 220 to 280 μm.

In the vicinity of the first natural frequency, displacement intensely increases and reaches nearly 1.8 mm and thereafter with increasing frequency, the blade tip displacement again decreases intensively.

According to Fig. 10, the resonance condition is imminent when the blade has been excited to a frequency of 550 Hz, that is, near to the first natural frequency. The blade will have been vibrated intensely in this condition and as shown in Fig. 11, the von Mises stress at sensitive spaces of blade (bade root) reaches 236 MPa.

Referring to Table 2, it is obvious that tension with an amount of 236 MPa is far less than any mechanical strength of an alloy except in the fatigue endurance limit, in other words, the blade material should be able to endure any forced statistical loads even at resonance state.

The maximum amount of von Mises stress is larger (68%) than fatigue endurance limit [8, 11] (236 MPa $>$ 140 MPa), therefore, when the blade encounters the fatigue condition at resonance state, the 19°-blade is not be able to endure the fatigue condition infinitely and blade fracture will be unavoidable.

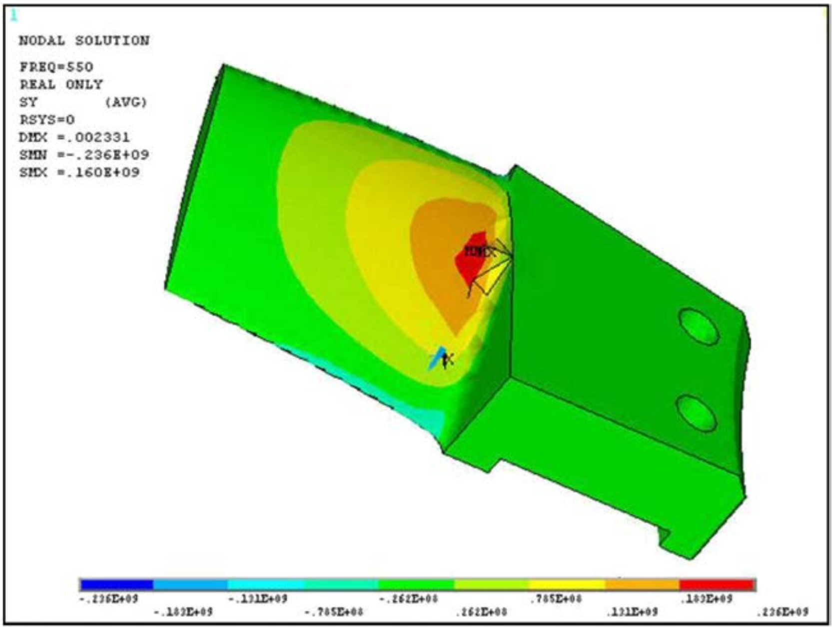

Fig. 11. Contours of the computed Von Mises stress distribution on 19°-blade at a frequency of 550 Hz.

3.2.4. Harmonic analysis for 14°-blade. From CFD analysis the force acting by air flow on the 14°-blade was calculated to be about 276.5 N. By acting these external forces on the blade at various frequencies (between 0 to 800 Hz), the blade-tip displacement is accounted with finite element analysis. The blade-tip displacement for these conditions is shown in Fig. 12.

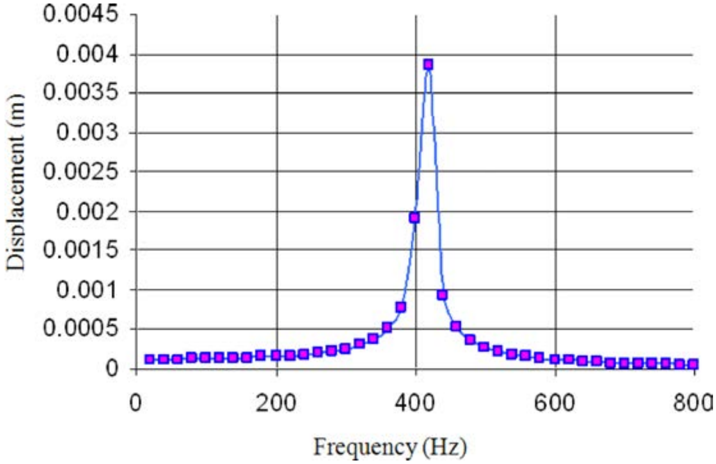

Fig. 12. 14°-blade-tip displacement at various frequencies in first mode of vibration.

As seen, at a frequency of 420 Hz the blade tip displacement reaches a maximum quantity (about 4 mm) because the frequency of 420 Hz is the closest value to the first natural frequency of 14°-blade (413.49 Hz). This amount of displacement (4 mm) is even more than for the 19°-blade in the vicinity of its first natural frequency (1.8 mm).

Notice from Fig. 12 that the frequency resonance condition happening at 420 Hz is imminent. The blade will be vibrated intensively in this condition and, as seen in Fig. 13, the von Mises stress at sensitive spaces of the blade (blade root) reaches 388 MPa. So again when the 14°-blade encounters the fatigue condition at resonance state, it was not be able to endure the fatigue condition infinitely and blade fracture will be unavoidable.

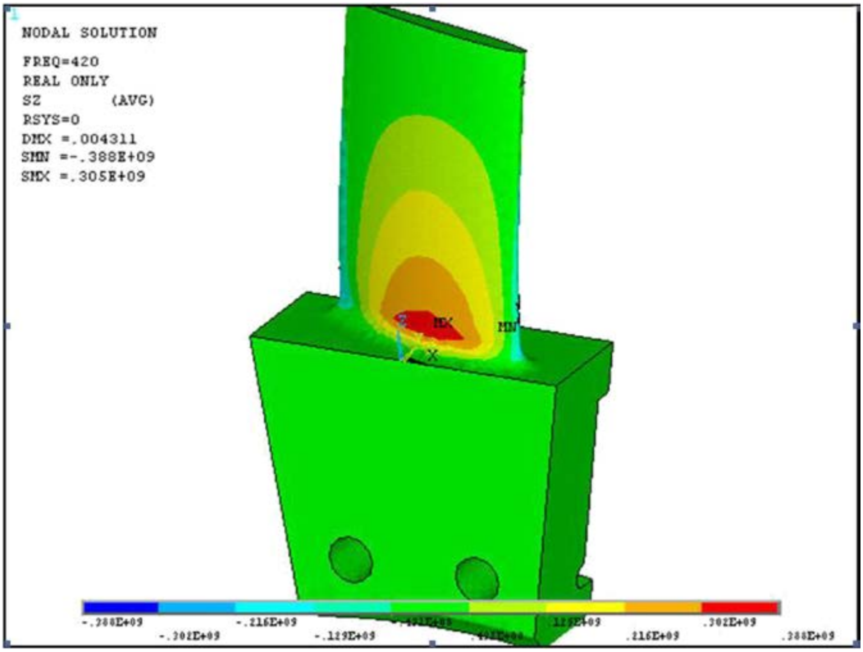

Fig. 13. Contour of computed von Mises stress distribution on a 14°-blade at a frequency of 550 Hz.

Nevertheless, as seen in Fig. 10, when the blade is excited at a frequency of 550 Hz, which is the frequency of the exciting force caused by shaft rotation, the 14°-blade tip displacement, will be less than 160 μm. Therefore, the resonance state will have not happened in this situation and the von Mises stress encountered by the 14°-blade root will be less than 10 MPa, which is small enough to be negligible. Blade failure will never been occurred for the 14°-blade in this situation.

4. Results and discussions

The results listed below have been taken from visual inspection and reports.

Measured dynamic stresses at 3000 rpm, (50 Hz frequency of power plant generators) for both 14° and 19°-blades, [5] compared with the yield stresses (presented in Table 2) and show that the stresses imposed on the blade are much lower than yield stresses and therefore there is no possibility of blade failure in normal operating conditions.

Cracking started from one or more points at the middle of the concave surface of the blade (having higher roughness can cause the crack on the surface of the blade) and this may be a reason to take the blade apart. The mentioned problem results from the effect of oscillatory loading being applied to the blade.

By changing the attack angle of the blades to 14°, no failures were observed. However, the rising of temperature in the generator casing was higher than 19°-blades. This results from a lower rate of sucked air flow for generator cooling for the 14°-blades. Since both type of blade are installed on the same shaft of the generator and rotate with the shaft, the fan rotation power is equal in both cases. However, the sucked air in the 14°-blade fan would be less than the other, and hence, the net power output is less and results in lower efficiency. For troubleshooting and to increase the sucked air flow for 14°-blades, using some extra guide blades has been proposed, as shown in Fig. 14.

Fig. 14. Extra guide blades for increasing the sucked air flow in the use of 14°-blades [5].

To investigate the cause of 19°-blades failure and having no failure in 14°-blades, SEM inspection and numerical analysis has been used as described below:

1. Study of ruptured surfaces by SEM and microstructure difference between fatigue failure and dimple rupture shows that there is no possibility of a collision of a large external object and its instantaneous rupture.

2. Distribution of flow, pressure and applied air flow forces on blades which have been modeled with CFD simulation, sustained that the forces were not enough to cause the blade rupture.
3. With respect to the obtained results from CFD and FEM, these analyses prove that the value of normal stress in most of conditions for 19° and 14°-blades is about 10 MPa, except for the resonance state.
4. In the case of applying a force with a frequency of around 550 Hz, the 19°-blade will be exposed to a resonance frequency (as a result of unsuitable blade installation, the resonance condition is probable) and because of applying stress at range of 160–236 MPa periodically and exceeds the endurance limit of the material (Al 2024 fatigue endurance limit $\sigma_e = 140$ MPa as presented in Table 2) will reduce the working life of the blade and cause failure after some cycles.
5. In the case of applying a force with a frequency of around 550 Hz, the 14°-blade will not be exposed to the resonance condition and because of applying stress at about 10 MPa, blade failure never occurs.

5. Conclusion

In accordance with the fracture of the 19°-blades, which occurred five times in the case of our study after overhaul and after less than 100 hr of operation, the investigation of the reason of fractures were necessary. By utilising a laboratory investigation (reports and SEM) and computational inspection (CFD and FEM), it is clear that the installation conditions (applied torque on bolts and nuts) were the main reason of failure.

To achieve a high accuracy in computations, the “ATOS” which is a new method based on 3D digital photography has been used for blades modeling. The results obtained from the CFD analysis have shown that the maximum stress, caused by rotation and air pressure forces on blades, is much lower than the material yield tensile strength.

Modal and harmonic analysis of the blade with FEM has indicated that the 19°-blades natural frequency is too close to the operational frequency of blades. It means that any changes in blade installation conditions cause the blade natural frequency to be similar to the operational frequency and consequently causes resonance phenomena. Because of the applied periodic stress that exceeds the endurance limit of the material, it will reduce working life of the blade and lead to failure after some cycles.

Study on fracture surfaces and results obtained from FEM show that the fracture of 19°-blades occurs in accordance with fatigue where there is resonance phenomena and crack propagation.

The natural frequency of the 14°-blades is not close to the blade's operational frequency and thus will not be exposed to a resonance condition and because of applying stress about 10 MPa, blade failure never occurs.

Acknowledgment

The authors gratefully acknowledge the office of gifted students of Semnan University for financial support.

References

1. Alsthom Company report in conjunction with some Gas Power Plants (1997).
2. Anderson L., *Fracture mechanics fundamental and applications,* CRC Press, 9780849316562, Colorado, USA (1995).
3. Barlow K.W., Chandra R., *Fatigue crack propagation simulation in an aircraft engine fan blade attachment*, Int. J. Fatigue, **27**, 1661–1668, 2005.
4. Beisheim J.R., Sinclair G.B., *On the three-dimensional finite element analysis of dovetail attachment*, [in:] *Proceedings of ASME Turbo Expo* 2002, Amsterdam, The Netherlands (2002).
5. Failure analysis report of Iran-Montazer-Ghaem units 2, 4 & 6. Iran Power Plant Repair Co, (2003–2004).
6. Hou J., Bryon J.W., Ross A., *An investigation of fatigue failures of turbine blades in a gas turbine engine by mechanical analysis*, Engineering Failure Analysis, **9**, 201–211, 2002.
7. Hutson A., Nicholas T., Johnc R., *Fretting fatigue crack analysis in Ti-6Al-4V*, Int. J. Fatigue, **27**, 1582–1589, 2005.
8. Joseph R., *ASM Specialty Handbook*, Aluminum and aluminum Alloys, ASM International, 087170496X, USA (1993).
9. Moussavi Torshizi S.E., Yadavar Nikravesh S.M., Jahangiri A., *Failure analysis of gas turbine generator cooling fan blades*, Engineering Failure Analysis, **16**, 1686–1695, 2009.
10. Paris P.C., Gomez M.P., Anderson W.E., *A rational analytical theory of fatigue*, Trend Eng., **13**, 1, 9–14, 1961.
11. Poursaeidi E., Salavatian M., *Failure analysis of generator rotor fan blades*, Engineering Failure Analysis, **14**, 851–860, 2007.
12. Poursaeidi E., Salavatian M., *Fatigue crack growth simulation in a generator fan blade*, Engineering Failure Analysis, **16**, 888–898, 2009.
13. Xi N.S., Zhong P.D., Huang H.Q., Yan H., Tao C.H., *Failure investigation of blade and disk in first stage compressor*, Eng. Fail Anal., **7**, 385–392.
14. http://www.cfg.cornell.edu/software/software.htm.

Received June 12, 2012; revised version February 2, 2013.

ENGINEERING TRANSACTIONS • *Engng. Trans.* • **61**, 2, 119–136, 2013
Polish Academy of Sciences • Institute of Fundamental Technological Research (IPPT PAN)
National Engineering School of Metz (ENIM)

An Experimental Study on Rate Sensitivity of J-Integral and its Evaluation by Small Punch Test for TRIP Steel

Leishi SHI[1], Takeshi IWAMOTO[2], Shinya HASHIMOTO[3]

[1] *Graduate School of Engineering, Hiroshima University*
1-4-1 Kagamiyama, Higashi-Hiroshima, Hiroshima, 739-8527 Japan
e-mail: m124742@hiroshima-u.ac.jp

[2] *Institute of Engineering, Hiroshima University*
1-4-1 Kagamiyama, Higashi-Hiroshima, Hiroshima, 739-8527 Japan

[3] *SUZUKI Motor Corporation*
300 Takatsuka, Minami, Hamamatsu, 432-8611 Japan

Recently, much attention has been paid to TRIP steel since it indicates both high ductility and strength by strain induced martensitic transformation. This transformation allows TRIP steel to offer larger energy absorption than other steel at the same strength level. Therefore, it is expected to be applied to automobiles as security components that absorb energy upon collision. To produce the best performance of TRIP steel, the J-integral of TRIP steel should be investigated with respect to a various deformation rates for an evaluation of energy absorption. In the present study, the three point bending (3B) test is conducted for investigating the J-integral until the crack growth of TRIP steel. Then, in order to determine the energy absorption characteristic by the J-integral value at various locations in the components of TRIP steel, the size of the specimen should be very small. Thus, an SP test is introduced and conducted by using the newly established apparatus based on the SHPB method. By using the result of the SP test in conjunction with the result of a 3B test, the evaluation of the J-integral of TRIP steel subject to various deflection rates is attempted. The correlation between the J-integral and the equivalent fracture strain of the SP test for TRIP steel is challenged to be redefined.

Key words: TRIP steel, energy absorption, J-integral, rate sensitivity, small punch test, SHPB method.

1. Introduction

TRIP steel indicates high ductility, toughness and excellent energy absorption under plastic deformation by strain-induced martensitic transformation (SIMT) [1]. Recently, in order to improve passenger safety and reduce weight of the car, the requirement of higher strength and excellent energy absorption of the steel used in the automobile industry has increased. Therefore, TRIP steel is expected to apply for the components which absorb energy upon collision.

Generally, the energy absorption is evaluated by calculating the area of the stress-strain curve obtained from the tensile test [2]. From this point of view, TOMITA and IWAMOTO [2] reported that energy absorption in TRIP steel decreases with an increase in strain rate. However, the dominant mechanism of those components for energy absorption is plastic-buckling with bending deformation. Due to a variety of impact velocity at the moment of the crash, the energy absorption characteristic of TRIP steel subjected to various rates of bending deflection becomes more important for a final product of the components. As RICE [3] defined, the J-integral can represent the total energy until the crack extension with its standardized experimental evaluation under the bending deformation. Over the past decade, the dynamic fracture toughness of steel is actively investigated [4] and a lot of investigations about the effect of rate sensitivity on mild steel have been done [5–7]; however, just a few studies on the fracture energy absorption sensitivity of the TRIP steel to the strain rate in experiment can be found [8, 9], especially under tension. In addition, just the clarification of its fracture energy absorption rate sensitivity for TRIP steel is insufficient. The residual stress and plastic strain in each location of the component are different, and SIMT will take place during the processing. In order to enhance and control the reliability and the performance of the product, the specimen picked out from the product should be very small to evaluate its characteristics.

In the past, several efforts have been made for the evaluation of energy absorption characteristics in metallic materials by the fracture parameters including the J-integral under static to dynamic loading based on the split Hopkinson pressure bar (SHPB) method [5, 10]. Especially, the fracture parameters of TRIP steel have been measured under quasi-static and impact tests [11, 12]. For studies by using the smaller specimen, a small punch (SP) test is well-employed to evaluate the J-integral [13–17]. By using this technique, the energy absorption for the part of the actual product of security components with respected to various deflection rate can be easily evaluated by a simple experiment. SHINDO *et al.* [14, 17] assessed the correlations between the equivalent fracture strain and the J-integral. In addition, they determined the J-integral in austenitic stainless steel, a kind of TRIP steel, and its weldment by combination between the SP test and FEA method. However, most of them are conducted under the low strain rate.

Due to the high impact velocity during the crash, it is important to clarify the energy absorption characteristic subjected to higher strain rate and its rate sensitivity by evaluating the J-integral by an SP test. Additionally, Rodriguez-Martinez *et al.* [18] examined the behavior of AISI 304 steel sheets, which is a kind of TRIP steel, subjected to perforation under a wide range of impact velocities. The result shows the work hardening and ductility of AISI 304 are enhanced and the absorbing energy capability of AISI 304 is improved by SIMT during perforation. They are distinguishing the plastic deformation from the fracture characteristic for energy absorption. From the viewpoint of the SP test, it can be considered that the perforation can be connecting to the fracture characteristic.

In the present study, at first, the three-point bending (3B) test of pre-cracked specimen based on the ASTM standard is conducted for various deflection rates. Then, the J-integral associated with the crack growth is measured during a 3B test by the direct current potential difference method. After that, an impact SP apparatus base on the classical SHPB method is newly established. The load-deflection curves of SP test subject to various deflection rates are obtained by the conventional material testing machine, weight drop testing machine and the established SHPB apparatus, in conjunction with the results of the 3B test, evaluation of the energy absorption characteristic of TRIP steel by the J-integral is attempted. The relationship between the J-integral and the equivalent fracture strain of the SP test is challenged to be redefined for various deflection rates. Finally, a rate sensitivity of energy absorption in TRIP steel is discussed.

2. Three point bending test (3B)

2.1. *Method of three point bending test (3B)*

In order to evaluate the J-integral before crack initiation, it is essential to find the point of the crack initiation on the load-deflection curve. Therefore, in this investigation, a direct current potential difference (DCPD) technique is introduced.

The DCPD method is one of the most accurate and efficient methods for monitoring the crack initiation and propagation in real time during deformation. By applying current to the specimen, the electrical potential difference between the crack faces is generated. A crack initiation is considered to be coincident with a sudden increase in potential difference. As the crack initiates, the resistance will be increased. This leads to an increased potential difference. As shown in Fig. 1. The load-time and voltage-time curve can be recorded and the moment when the voltage suddenly increased is defined as the point of crack initiation [19].

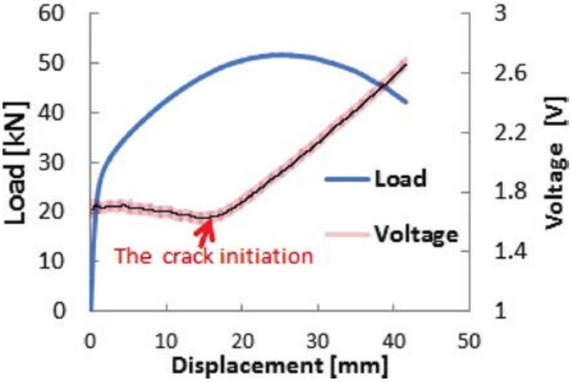

FIG. 1. An example of a result obtained by the DCPD method to determine the point of crack initiation.

2.2. Samples used for 3B test

Pre-cracked specimens made of AISI304, a kind of TRIP steel, are used in this test. The dimensions of the pre-cracked specimen follow the ASTM standard as shown in Fig. 2. To get an austenitic structure, the specimen is subjected to solution heat treatment at 1323K for 30 min by electric furnaces and then quenched in water.

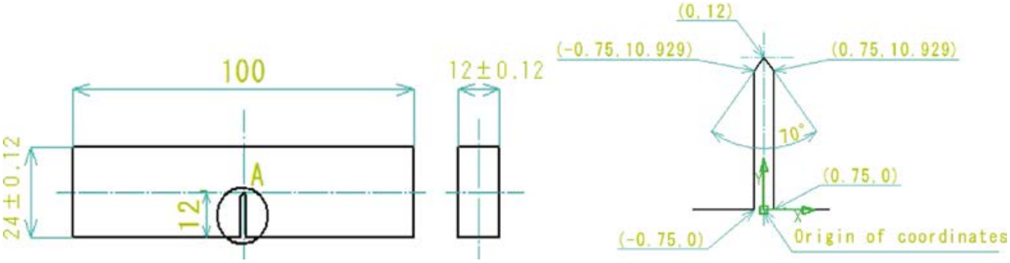

FIG. 2. The dimensions of the specimen for 3B test.

2.3. Measurement apparatus of 3B test

Figure 3 shows the schematic diagram of the locations of probes for measuring voltage and supplying current. Two probes that are independent of the current supplement are used to measure the voltage. The circuit is based on the four-probe method for precise measurement of voltages. In order to make the probes as sensitive as possible, they are fixed around the pre-crack on the opposite side in the thickness direction of the specimen. The current supplied wire and the probes for measuring the voltage are spot-welded to the specimen. The current is set as 12 A.

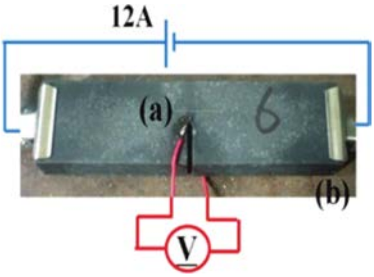

FIG. 3. A photograph of the specimen with some drawings of the circuit to show locations of the probes for measuring voltage and supplying current.

In the quasi-static test, the signal from the signal conditioner (Kyowa CDV-700A) for recording the potential difference is put into the conventional material testing machine (Shimadzu AG-250kNXplus), which is shown in Fig. 4. The speeds of crosshead are set as 0.2, 2, 20 and 200 mm/min. The relationship of load-displacement and potential-difference-displacement are recorded simultaneously.

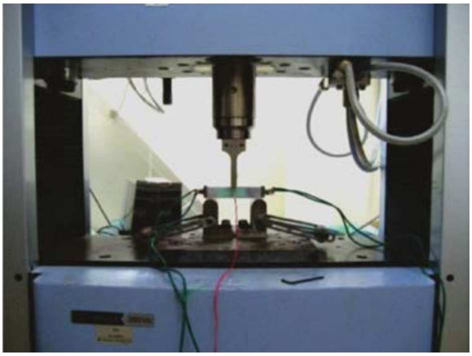

FIG. 4. The photograph of the quasi-static three-point bending test apparatus.

Figure 5 shows the schematic illustration and a photograph of the drop weight testing setup. In this test, the load and potential difference are recorded by the oscilloscope (Yokogawa DL-2700) at the same time. A load sensing block [20] which can capture the load and protect the reflected wave propagates back into the load sensing part set just under the center. Figure 6 shows a photograph of the load sensing block used in the present study. The load sensing block has a small projection. Two strain gauges are glued axisymmetrically at the middle of the projection. These two strain gauges are connected to a digital oscilloscope (Yokogawa DL-2700) via a signal conditioner (Kyowa CDV-700A) for amplifying the voltage signal. According to the relationship between voltage and load calibrated by using the material testing machine, a voltage-time curve can be transform into a load-time curve. Weight is dropped from a height of

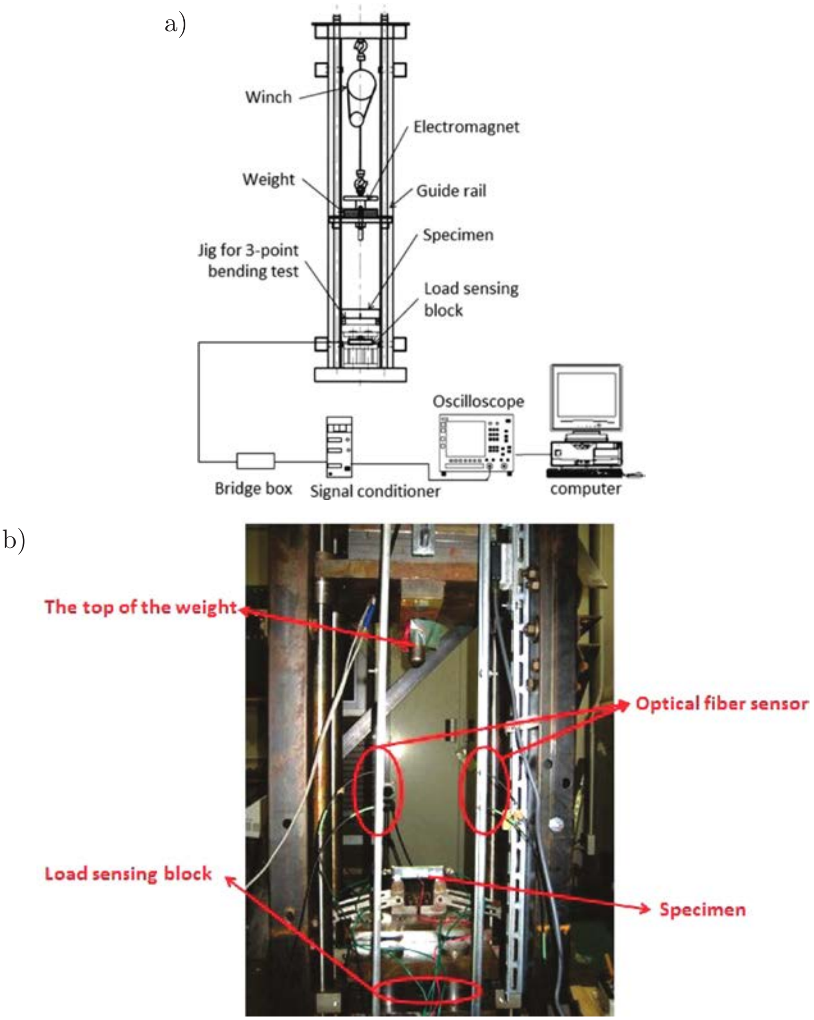

FIG. 5. a) A schematic and b) a photograph of the drop weight test setup.

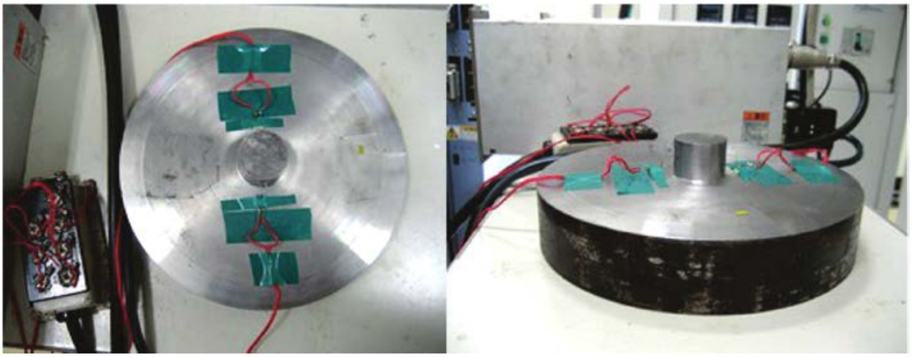

FIG. 6. The photograph of the load sensing block used in drop weight test.

700 mm and 900 mm respectively. The deflection with respect to time is recorded by a high speed camera during impact. The deflection rate can be calculated from a deflection-time curve by the finite difference method. The corresponding deflection rates in the impact are approximately 3190 mm/s and 3530 mm/s. The normalized deflection rates can be calculated as 40 s^{-1} and 45 s^{-1} divided by the span length of 80 mm, respectively.

2.4. The manner of data processing

In this investigation the simple formula for evaluating the J-integral under bending deformation derived by Rice [21] is used. The formula is given by the following equation.

$$J = \frac{Af(a_0/W)}{B(W-a)}, \tag{2.1}$$

where A is the area under the load-deflection curve up to the point of crack initiation. It can be calculated by using the DCPD method as described in Subsec. 2.1. B and W are the initial thickness and width of the specimen respectively. a is the initial crack length including the notch and the fatigue pre-crack. Since the aim of this investigation is to evaluate the energy absorption characteristic of TRIP steel with an extremely high ductility. The dimensions of the specimen are based on the ASTM standard. Therefore a is equal to 14.4 mm and a value of two for $f(a_0/W)$ is employed.

2.5. Discussion on the result of 3B test

Figure 7 shows the relationship between the J-integral and the normalized deflection obtained from the 3B test. It presents an approximately linear rela-

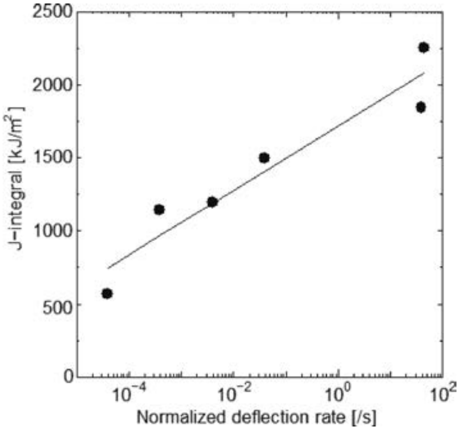

Fig. 7. Relationship between the J-integral and the normalized deflection rate of 3B test.

tionship between the J-integral and the normalized deflection rate on the semi-logarithmic plot. A positive rate-sensitivity can be observed by the J-integral value's increase with an increase in the deflection rate.

3. Small punch test

3.1. Samples used for small punch test

Two kinds of material are employed in this test, aluminum alloy 6061 and AISI304. The aluminum alloy specimen is used for confirming the validity of the established apparatus for SP test under quasi-static test. Both of them are machined to a disk shape and they both have dimensions of 10 mm in diameter and 0.5 mm in thickness. The specimen, made of AISI304, is subjected to solution heat treatment at 1323K for 30 minutes by electric furnaces and then quenched in water.

3.2. Measurement apparatus

3.2.1. The SP test apparatus for quasi-static SP test. Figure 8 shows the established apparatus for the quasi-static SP test and the schematic figure of jigs for both quasi-static and drop weight SP test. It consists of upper and lower dies, four clamping screws and a puncher. In order to keep the centers of the punch, specimen and dies in as a straight a line as possible, a cylindrical collar is employed here. In order to prevent the specimen being subjected to frictional

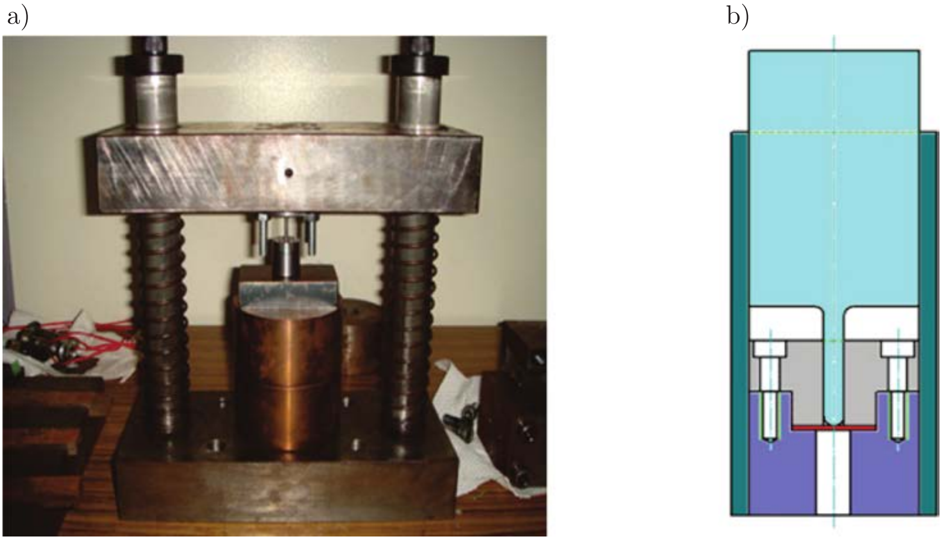

Fig. 8. a) The established apparatus for the quasi-static SP test and b) a schematic of jigs for both quasi-static and drop weight SP test.

forces during deformation, the bore diameter in the lower dies is determined as follows [22]

$$d_2 \geq d_1 + 2t_0, \tag{3.1}$$

where d_1, d_2 and t_0 are the outer diameter of the lower die, the inner diameter of the upper die and the original thickness of the specimen respectively. In present study, d_1 is decided as 2.4 mm and d_2 is decided as 4 mm.

The quasi-static test is conducted with a conventional material testing machine, and the crosshead speeds are set as 0.2, 2, 20 and 200 mm/min.

3.2.2. Confirm the validity of the apparatus. In order to confirm the validity of the apparatus which was established for SP test, the SP test is conducted by the same setup and condition with past research work [16]. Figure 9 shows the comparison of the load-deflection curves under quasi-static test obtained by the present study and the previous study. The result of the present study coincide with the previous study, and so, we can find that the apparatus manufactured here is valid.

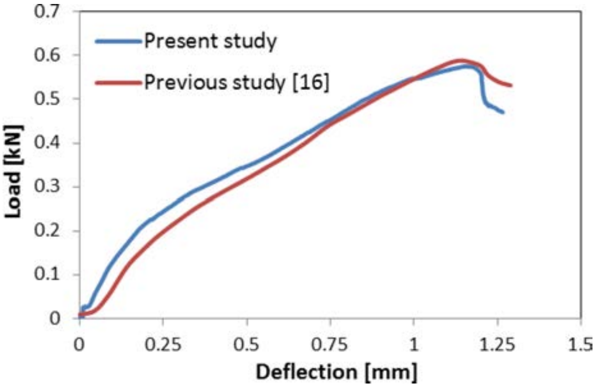

FIG. 9. The comparison of the load-deflection curves obtained by the present study and a previous study [16].

3.2.3. The SP test apparatus based on the drop weight method. The jig for SP test based on the drop weight method is shown in Fig. 10. The SP test apparatus is placed on the center of the steel plate. Weight is dropped from a height of 20 mm. The speed of the weight at the moment of impact can be calculated by using two optical fiber sensors. A gauge line is marked on the top of the puncher. By tracking the position of the gauge line with the high speed camera, the displacement with respect to the time of the punch can be obtained as shown in Fig. 11a. The load during the impact can be recorded by the load sensor block which is as same as the drop weight 3B test is shown in Fig. 11b.

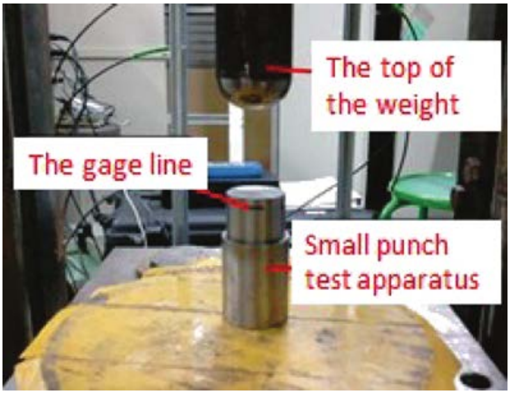

FIG. 10. The jig used for SP test based on the drop weight test method.

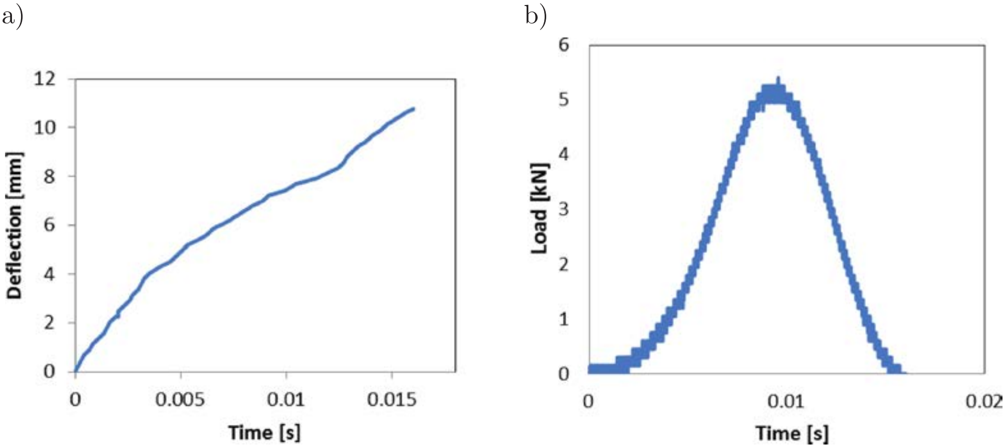

FIG. 11. The deflection-time curve (a) and load-time curve (b) obtained by SP test based on drop weight test method.

3.2.4. The impact SP test based on SHPB method. To conduct the impact SP test under high loading speed, an impact SP test apparatus is newly established based on the SHPB method. The schematic picture of the established apparatus is shown in Fig. 12. It consists of an air gun, a striker bar, an input bar, an output tube and some measurement devices. The puncher and the lower die are directly manufactured at the ends of the input bar and the output tube respectively. The upper die is connected to lower die with the output tube by a thread and the specimen is clamped between the upper die and the output tube. A collar with lower mechanical impedance is used to keep straightness of the center of the punch and the specimen. The dimensions of this apparatus are also designed by Eq. (3.1). When the air gun launches the striker bar to impact on the edge of input bar by a sudden release of compressed air, a stress pulse is generated and propagated along the input bar toward the specimen. After it arrived the specimen, partially of it reflected back into the input bar as the reflected strain pulse, and the residual pulse transmitted though the specimen into the output bar as the transmitted strain pulse. To record the strain wave in the pressure bar and tube, the semi-conductor strain gauges (Kyowa KSP-z-120-E4) are glued axisymmetrically at the middle of the pressure bar and tube. All strain gages are connected to a digital oscilloscope (Yokogawa DL-2700) via signal conditioner (Kyowa CDV-700A) for amplifying the voltage signal.

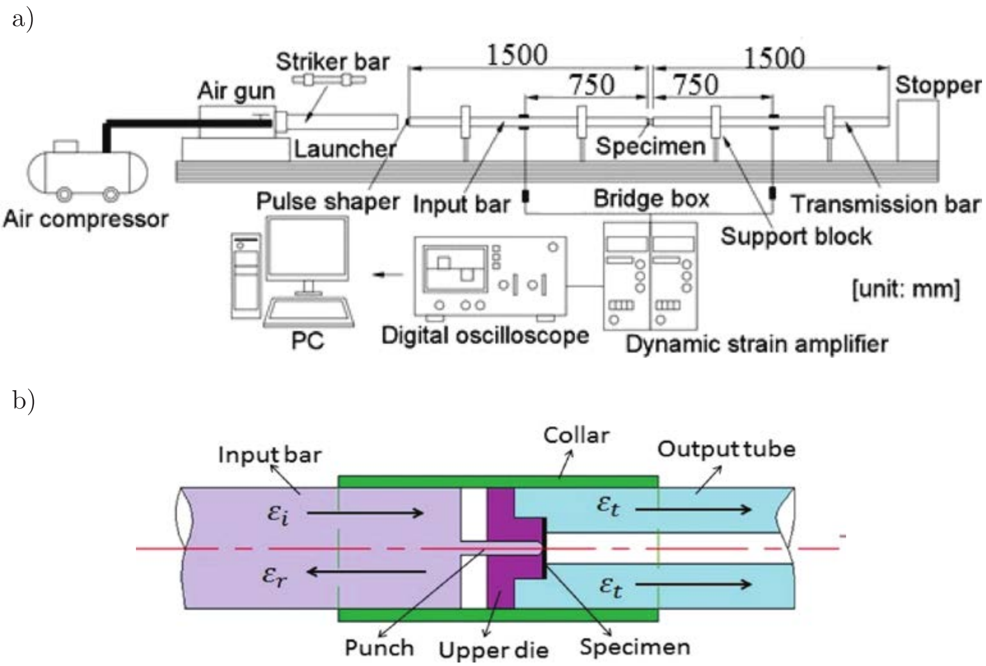

FIG. 12. The schematic picture of the established apparatus for the SP test based on SHPB method: a) whole of the apparatus; b) near the specimen including upper die and collar.

The stress pulses propagating through the incident and transmitter bars, σ_i, σ_r, σ_t can be obtained respectively. Obeying the one-dimensional elastic wave propagation theory, particle velocities in the incident and transmitter bars v_{in} and v_{out} can be obtained by the following equation.

$$\begin{aligned} v_{\text{inp}}(t) &= \frac{\sigma_i(t) - \sigma_r(t)}{\rho c}, \\ v_{\text{out}}(t) &= \frac{\sigma_t(t)}{\rho c}, \end{aligned} \tag{3.2}$$

where ρ and c are mass density and velocity of longitudinal elastic wave in pressure bars. Using the following equation, a deflection at the center of the specimen $\delta(t)$ is calculated as

$$\delta(t) = \int_0^t \{v_{\text{inp}}(t) - v_{\text{out}}(t)\}\, dt'. \tag{3.3}$$

According to results above, the input load $P_{\text{inp}}(t)$ and load at support point $P_{\text{sup}}(t)$ can be calculated by the follow equation:

$$P_{\text{inp}}(t) = [\sigma_i(t) + \sigma_r(t)]\, A_{\text{in}}, \qquad P_{\text{sup}}(t) = \sigma_t(t) A_{\text{out}}, \tag{3.4}$$

where A_{in} is the cross-sectional area of the input bar and A_{out} is the cross-sectional area of the output bar. In general, the stress wave obtained by SHPB method has the initial oscillation. To reduce the initial oscillation, the pulse shaper technique was introduced [23, 24].

3.3. The manner of data processing

In the present study, the J-integral is calculated by using the method proposed by SHINDO *et al.* [17]. The determination process of the evaluation equation is given as follows.

At first, the equivalent fracture strain, which is very important in order to obtain the J-integral of the SP test, is derived by using the follow equation under the assumption of constant volume during plastic deformation:

$$\bar{\varepsilon}_{qf} = \ln\left(\frac{t_0}{t}\right), \tag{3.5}$$

where t_0 is the initial thickness of specimen and t is the thickness of the fracture part measured after the experiment. In the present study, t_0 is equal to 0.5 mm and t in the part of the fracture on the specimen is measured by using a micrometer. The plotted relationship between $\ln(\ln(t_0/t))$ and $\ln(\delta_{\max}/t_0)$ have an approximate linear relationship. Therefore, we can obtain the following equation,

$$\bar{\varepsilon}_{qf} = \alpha \left(\frac{\delta_{\max}}{t_0}\right)^n, \tag{3.6}$$

where t_0 is the initial thickness of specimen, $\delta_{\max}$ is the deflection at the maximum load obtained by the load-deflection curve from the SP test. From the correlation between $\ln(\ln(t_0/t))$ and $\ln(\delta_{\max}/t_0)$, α and n can be identified. Then according to the method by SHINDO *et al.* [17], the J-integral obtained by experimental results of the J-integral using CT specimen has an approximate linear relationship with equivalent fracture strain which obtained by SP test at same deflection rate. The linear equation can be obtained as follows:

$$J_{\text{in}} = A\bar{\varepsilon}_{qf} - B, \tag{3.7}$$

where A and B are parameters, respectively.

3.4. Discussion on the result of SP test

Figure 13 shows the load-deflection curve at the various deflection rate obtained by the SP test. As shown in this figure, the deflection at the maximum load increases with an increasing deflection rate. Generally, in the conventional tensile test for the metallic material, the load increases with an increase of strain rates. At the same time, the maximum strain for failure becomes lower with an increase of the strain rate. This implies that the strength becomes larger, but the ductility decreases with respect to the strain rate. However, in the present study an opposite tendency on the rate sensitivity of the deflection is observed.

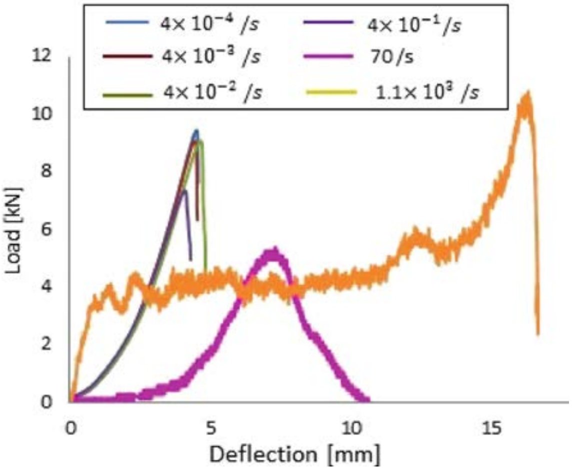

FIG. 13. Load-deflection curves at various deflection rates.

Figure 14 shows the stress waves captured from the impact SP test based on the SHPB method. Here it is observed that transmitted wave is quite small compared with the incident and reflected waves. This phenomenon may be caused by the stress wave becoming quite small when it is transmitted to the output tube. Since the cross-section area may be large relative to the cross-section area of the punch, most of the stress wave is reflected when the punch hits the specimen

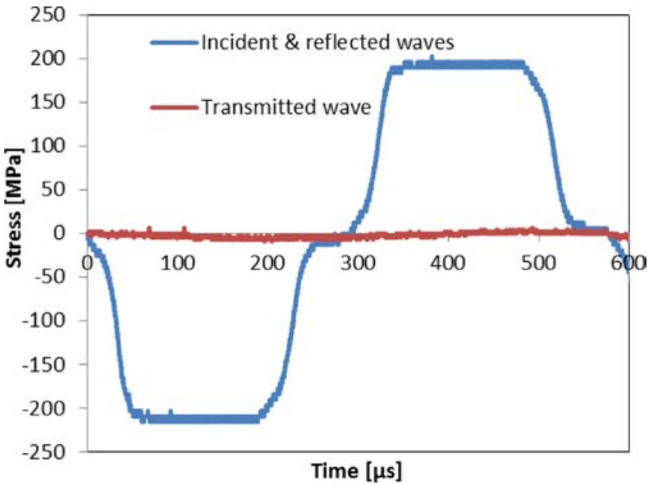

FIG. 14. Incident, reflected and transmitted pulse obtained from impact small punch testing.

and the load turn to smaller. In addition, the fiction between the punch and the specimen maybe created during the impact. It leads a partial of incident stress consumed during the fracture process. However, the load and deflection still can be calculated because the signal itself can be captured by an appropriate adjustment of the resolution in output voltage.

4. DISCUSSION ON THE RESULT OF THE WHOLE WORK

Following the steps described in the Subsec. 3.3, the approximately linear relationship between $\ln(\ln(t_0/t))$ and $\ln(\delta_{\max}/t_0)$, and the relation between the J-integral and fracture strain can be obtained as shown in Fig. 15 and the parameters of Eq. (3.6) and Eq. (3.7) are identified by these two relationship. The final equations are shown as follow.

$$\overline{\varepsilon}_{qf} = 0.001\left(\frac{\delta_{\max}}{t_0}\right)^{2.54}, \tag{4.1}$$

$$J = 1970\overline{\varepsilon}_{qf} + 633. \tag{4.2}$$

Unfortunately, as shown in Fig. 15b, it is hard to describe the corresponding J-integral for the result of the SP test based on the SHPB method. However, the maximum load of the SP test based on the SHPB method is known. Therefore, it is allowed that the J-integral at such higher deflection rate can be calculated by using above two equations and it becomes approximately 7922 kJ/m^2. Nevertheless, according to the approximate linear relationship which obtained

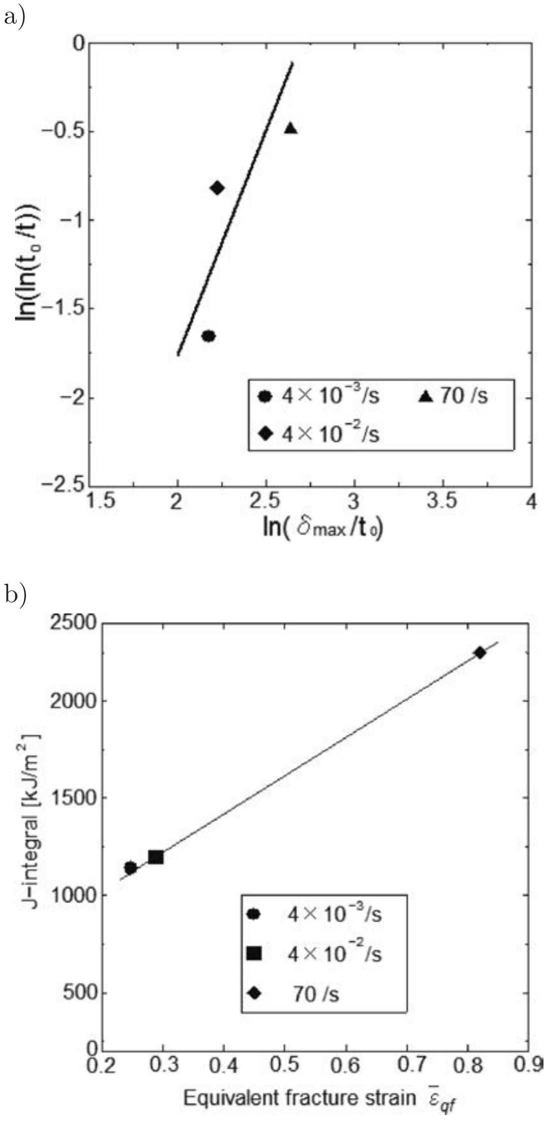

FIG. 15. a) The approximately linear relationship between $\ln(\ln(t/t))$ and $\ln(\delta_{\max}/t_0)$, b) the relation between the Jintegral and equivalent fracture strain.

from Fig. 7, the J-integral of 3B test base on SHPB method should be approximately 2456 kJ/m^2. Therefore, we can conject that the J-integral may be not have a linear relationship with normalized deflection rate under high strain rates anymore. This means that a different mechanism for energy absorption occurs in the range of higher deflection rate compared with the result of the 3B test by the drop weight machine.

In the previous study [17], the parameters for the Eq. (3.6) and Eq. (3.7) have been identified for austenitic stainless steel at the cryogenic temperature. Here, in order to compare this with the relations defined by the previous study [17], the J-integral is calculated using their parameters and $\delta_{\max}$ of the results in present study. The result is shown in Fig. 16. Compare with the result shown in Fig. 7 the values of J-integral are approximately four times the results obtained by 3B test at the same deflection rate. Taking into consideration that the equations by Shindo *et al.* [17] are defined at the cryogenic temperature, the J-integral value maybe overestimated.

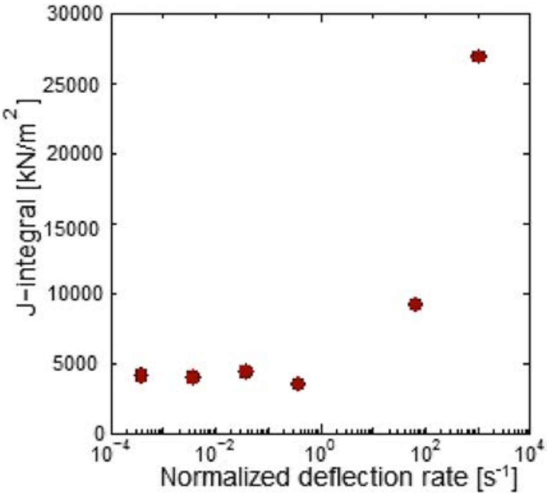

Fig. 16. The relationship between the J-integral and normalized deflection rate.

In the present study, a relationship between the energy absorption characteristic up to crack initiation and the normalized deflection rate was obtained by J-integral. The apparatus for impact SP test based on the modified SPBH method was established. By using the result of the 3B test, the relation between J-integral and the equivalent fracture strain under the SP test was redefined. Finally, the fracture energy absorption of SP test obtained by SHPB method was calculated. An experimental method for studying the rate sensitivity of energy absorption was established.

Acknowledgment

We gratefully acknowledge financial supports from a Grant-in-Aid for Scientific Research from the Ministry of Education, Culture, Sports, Science and Technology, Japan.

References

1. Zackay V.F., Parker E.R., Fahr D., Busch R., *The enhancement of ductility in high-strength steels*, Trans. ASM, Quart., **60**, 252–259, 1967.
2. Tomita Y., Iwamoto T., *Constitutive modeling of TRIP steel and its application to the improvement of mechanical properties*, Int. J. Mech. Sci., **37**, 12, 1295–1305, 1995.
3. Rice J.R., *A path independent integral and the approximate analysis of strain concentration by notches and cracks*, J. App. Mech., **35**, 379–386, 1968.
4. Kobayashi T., Yamamoto I., Niinomi M., *Evaluation of the dynamic fracture toughness parameters by instrumented charpy test* [in Japanese], Tetsu-to-Hagane, 16, 1934-1940, 1985.
5. Klepaczko J.R., *Discussion of a new experimental method in measuring fracture toughness initiation at high loading rates by stress waves*, J. Eng. Mater. Technol., Trans. of ASM, **104**, 1, 29–35, 1982.
6. Xu Z., Li Y., *Study of loading rate effect on dynamic fracture toughness of high strength steel under impact loading*, Streng. Fract. Compl., **6**, 1–2, 17–23, 2010.
7. Kalthoff J.F., *Fracture behavior under high rates of loading*, Eng. Fract. Mech., **23**, 1, 289–298, 1986.
8. Bleck W., Schael I., *Determination of crash-relevant material parameters by dynamic tensile tests*, Steel Research, **71**, 173–178, 2000.
9. Choi I.D., Bruce D.M., Kim S.J., Lee C.G., Park S.H., Matlock D.K., Speer J.G., *Deformation Behavior of Low Carbon TRIP Sheet Steels at High Strain Rates*, ISIJ Int. J., **42**, 12, 1483–1489, 2002.
10. Yokoyama T., Kishida K., *A novel impact three-point bend test method for determining dynamic fracture-initiation toughness*, Exp. Mech., **29**, 2, 188–194, 1989.
11. Kobayashi T., Wakai N., Yagi W., Kazino T., Ueda Y., *Effects of manganese and nickel increase on mechanical properties of TRIP Steel* [in Japanese], Tetsu-to-Hagane, **71**, 9, 1178–1185, 1985.
12. Antolovich S.D., Singh B., *On the toughness increment associated with the austenite to martensite phase transformation in TRIP steels*, Metall. Mater. Trans. B, **2**, 8, 2135–2141, 1971
13. Mao X., Takahashi H., *Development of a further-miniaturized specimen of 3 mm diameter for tem disk small punch tests*, J. Nucl. Mater., **150**, 1, 42–52, 1987.
14. Shindo Y., Yamaguchi Y., Horiguchi K., *Small punch testing for determining the cryogenic fracture properties of 304 and 316 austenitic stainless steels in a high magnetic field*, Cryogenics, **44**, 11, 789–792, 2004.
15. Foulds J., Viswanathan R., *Small Punch Testing for Determining the Material Toughness of Low Alloy Steel Components in Service*, J. Eng. Mater. Technol., **116**, 4, 457–464, 1994.
16. Budzakoska E., Carr D.G., Stathers P.A., Li H., Harrison R.P., Hellier A.K., Yeung W.Y., *Predicting the Jintegral fracture toughness of Al 6061 using the small punch test*, Fat. Fract. Eng. Mater. Struct., **30**, 9, 796–807, 2007.

17. Shindo Y., Horiguchi K., Sugo T., Mano Y., *Finite element analysis and small punch testing for determining the cryogenic fracture toughness of austenitic stainless steel weld*, J. Test. Eval., **28**, 6, 431–437, 2000.

18. Rodriguez-Martinez J.A., Rusinek A., Pesci R., *Experimental survey on the behaviour of SISI 304 steel sheets subjected to perforation*, Thin-Walled Struct., **48**, 12, 966–978, 2010.

19. Brown W.F., Srawley J.E., *Fracture toughness testing*, ASTM Spec. Tech Publ., **381**, 175–180, 1965

20. Chuman Y., Mimura K., Kaizu K., Tanimura S., *A sensing block method for measuring impact force generated at a contact part*, Int. J. Impact Eng., **19**, 2, 165–174, 1997.

21. Rice J.R., Paris P.C., Merkle J.G, *Some further results of J-Integral analysis and estimates*, ASTM STP536, 231–245, 1973.

22. Mao X., Takahashi H., *Development of a further-miniaturized specimen of 3 mm diameter for TEM disk small punch tests*, J. Nuclear Materials, **150**, 42–52, 1987.

23. Nemat-Nasser S., Isaacs J.B., Starrett J.E., *Hopkinson Techniques for Dynamic Recovery Experiments*, Proc. Roy. Soc. Lond., A, **435**, 1894, 371–391, 1991.

24. Frew D.J., Forrestal M.J., Chen W., *Pulse Shaping Techniques for Testing Elastic-plastic Materials with a Split Hopkinson Pressure Bar*, Exp. Mech., **45**, 2, 186–195, 2005.

Received November 12, 2012; revised version March 5, 2013.

ENGINEERING TRANSACTIONS • *Engng. Trans.* • **61**, 2, 137–150, 2013
Polish Academy of Sciences • Institute of Fundamental Technological Research (IPPT PAN)
National Engineering School of Metz (ENIM)

Elastic Stresses in Thin-Walled Torsional Structures Designed with SADSF Method

Ireneusz MARKIEWICZ

Kielce University of Technology
al. Tysiąclecia Państwa Polskiego 7, 25-314 Kielce, Poland
e-mail: ireneusz.markiewicz@tu.kielce.pl

The paper presents general conclusions arising from FEM analyses of elastic properties of thin-walled structures designed with the application version of the statically admissible discontinuous stress fields (SADSF) method. The analyses have been carried out as a part of a large-scale research program, whose main objective is conclusive verification of practical usefulness of the SADSF method in design. The present state of development of the method's application software is so advanced that it allows one to design even very complicated thin-walled structures composed of plane elements. This is a particular class of structures to which the Saint Venant's principle is not applicable [3, 4], and the methods based on consecutive iterative improvements should be applied with due caution. In the SADSF method one does not use iterations, and the method can be applied already at the stage when only boundary conditions are known [3, 4]. Unfortunately, the method is an approximate one and does not apply to the elastic range of stress that usually exists in exploitation conditions.

On the basis of analyses carried out for several dozen cases of thin-walled structures designed with the SADSF method we can state, among other things, that in these structures there are dominating membrane states, deformations remain small, equivalent stress fields are well equalized also along free borders, stress concentrations are relatively low, and maximal levels of equivalent stresses are approximately the same in all component elements. It has also been proven that the structures designed with the SADSF method may have strength properties even several dozen times better that those of structures designed traditionally. The obtained conclusions are presented on the basis of three selected examples of original, which in this case have open-section structures (see e.g. [11]) designed to carry torsional load [3, 4].

Key words: design, thin-walled structures, limit load capacity, FEM analysis.

1. Introduction

The problem of designing structures that have good strength properties (good equalization of equivalent stress, low stress concentrations, *etc.*) and at the same time being light, have long been the centre of engineers' attention. The solutions satisfying these requirements are sought for in the class of thin-walled structures, and these are widely applied in practice (e.g., in automobiles and in various machine and building structures). However, they have specific properties. First of all, great sensitivity of their structural parameters to changes, and often apparently small ones, i.e. to the changes in number, spatial allocation and mutual connections of component elements [4]. In consequence, methods based on procedures of consecutive iterative improvements, among them also the advanced methods of so-called topological optimization [1], should be used for these structures with due care [3].

A method that does not rely on consecutive improvements and is easy to use for an engineer is one of Statically-Admissible Discontinuous Stress Fields (SADSF) [2, 3, 7, 8, 12–14]. The method is aimed at designing thin-walled structures composed of plane elements. One can use it already at the design stage, when only boundary conditions are known [3, 14].

A certain limitation of the SADSF method is that it is based on conclusions arising from the lower-bond theorem of limit analysis, and thus it is an approximate method. It assumes among other things, that one exclusively uses an rigid ideally-plastic model of material, a plane state of stress is realized in each component element, and that only the limit state of the structure is analysed which corresponds to the beginning of its collapse. For these reasons, since the method came into being in nineteen-sixties [12], researchers have carried out fragmentary investigations on properties of structures designed with the SADSF method. Initially, these were plane structures, later three-dimensional structures have also been examined [2–13]. The results of these investigations have shown good, sometimes even surprisingly good, load-carrying properties of SADSF structures in the whole range of applied loads including the elastic range – which usually is the range of working load. Unfortunately, because of a dissimilarity between the physical material models used for analyses in this range and those applied in the limit state, one can not prove that such properties would be encountered in all cases of structures designed with the SADSF method [2, 3, 12]. Nevertheless, having an adequately reach material from research confirming good properties of SADSF structures, one may regard such properties as the expected ones.

Therefore, the basic aim of the large-scale research program undertaken by the author has been recognition of actual properties of structures designed with the SADSF method and conclusive verification of the usefulness of the method in design. Having in mind large the scale of the investigations carried-out (a large number of structure cases) we have selected computational and experimental methods that are neither very onerous nor expensive.

In the course of the program we have investigated, among other things:

- distributions of elastic stress fields by means of FEM,
- development of plastic zones, examined using e.g. thermovision, and actual mechanisms of collapse and equilibrium paths,
- fatigue strength, determined by applying the local strain method.

Application of the FEM in the analyses of properties in the elastic range allowed us to relatively easily analyse practically all the interesting cases, known from literature [2–4, 14] of thin-walled structures designed with the SADSF method. Among them we have not found any negative example. Having at our disposal such an extensive research material we could assume that the good elastic properties, described in the following part of this work, are expected.

In this work, general conclusions arising from the aforementioned analyses are presented by example of three selected interesting structures whose proportions are similar to those of crossbars in carrying frames of vehicles (Fig. 1). The interesting detail is that, despite the fact that these structures consist of open sections they could be successfully designed for torsional loads. In this way it was proven once again that such profiles might have significant torsional rigidity, contrary to what was stipulated by simplified one-dimensional theories [3]. We have chosen these particular structures for presentation, the ones which belong to the "worst cases" encountered in our investigations. The reason is that in-plane bending loads appear there in most of the plane components, so that one can not expect good equalization of equivalent stress in large fragments of the structure's volume – contrary to what we observe in many other structures designed with the SADSF method (see for example [11]).

The structures were originally designed by W. Bodaszewski [3, 4] with the use of the software package SADSFaM1 developed by himself [3, 14].

An illustrative example of the formulation of a design problem is presented in Fig. 1a [3]. The only input data were: the limit load **S** and **T** applied to the segment S_p of the border S (which can be reduced to the limit moment $M_{gr} = S \cdot a - 2T \cdot h$), the geometry of the segment S_p (with dimensions: L, h, a, b, δ), and the plastic properties of the material of the sought-after structure (with yield point σ_Y).

The task was to design a statically-admissible stress field which satisfies the assumed boundary conditions, and – at each point of the structure – the assumed yield condition. Then, the contours of the field should be made identical to the contours of the sought-after structure [2, 3].

When using the application version of the method, one designs the structure by selecting ready-made particular solutions of the fields from a library (Fig. 1b), and connecting them while paying attention to satisfying the boundary conditions and equilibrium conditions at the places of connection. To perform this task, the designer should only know the fundamentals of statics and to show some inventiveness.

The solution to the problem from Fig. 1a, denoted as "F95b" (the same denotation as the file containing its data) is shown in Fig. 1c, while the method of

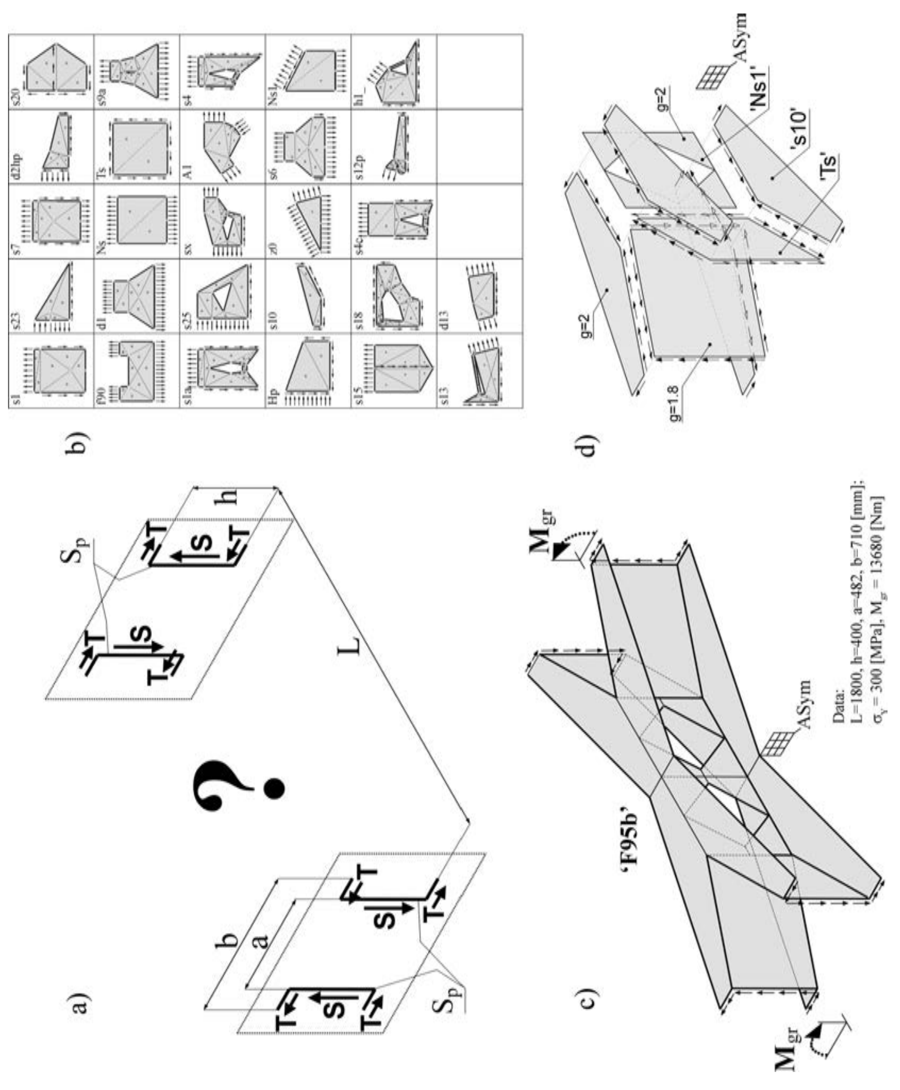
a)
b
a
h
L
?
S
T
S_p
b)
s1
s23
s7
d2hp
s20
f90
d1
Ns
Ts
s9a
s1a
s25
sx
A1
s4
Hp
s10
z0
s6
Ns1
s15
s18
s4c
s12p
h1
s13
d13
c)
'F95b'
M_{gr}
ASym
Data:
L=1800, h=400, a=482, b=710 [mm];
$\sigma_Y = 300$ [MPa], $M_{gr} = 13680$ [Nm]
d)
g=2
g=1.8
'Ns1'
's10'
'Ts'
ASym

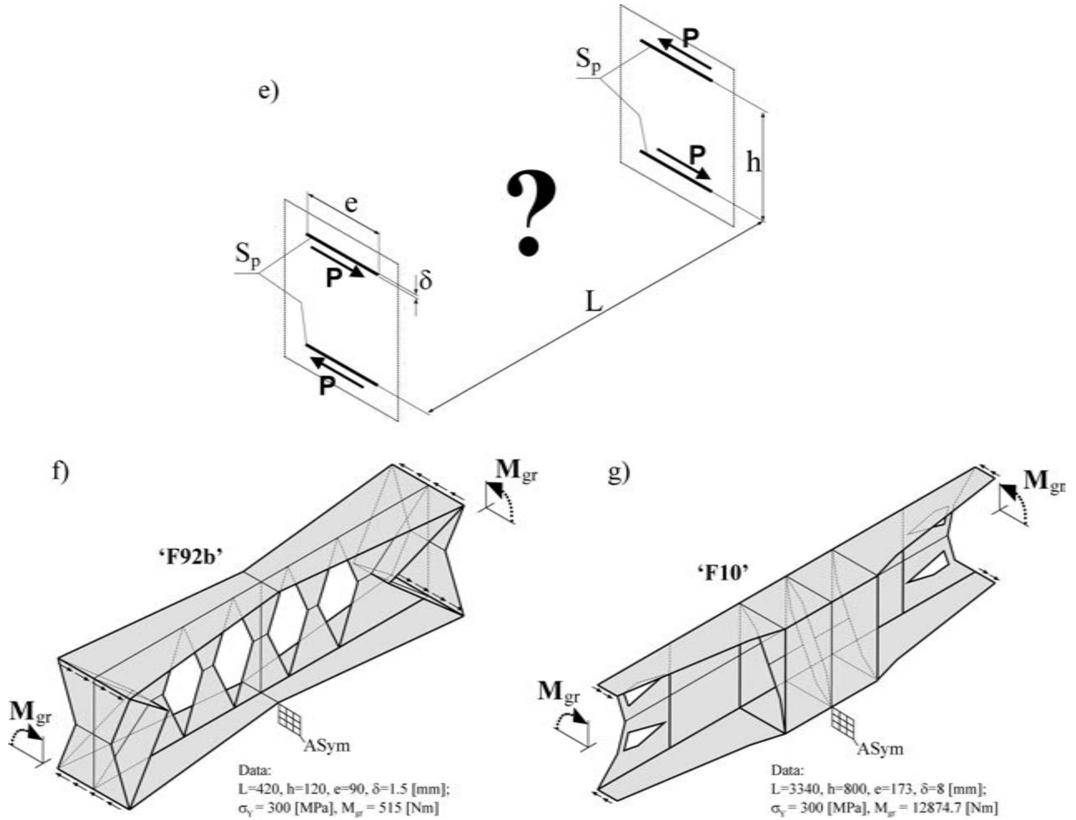

FIG. 1. Example formulations of design problems and contours of statically-admissible stress fields determining shape and dimensions of models of torsional structures analysed in work [4]: a) illustration of boundary conditions and problem formulation; b) library of ready-made solutions from the package SADSFaM1 [3, 14]; c) solution to the problem from Fig. 1a: statically-admissible complex spatial field, which determines contours of the structure; d) allocation of component library fields, and interactions between the fields in the antisymmetric half of the complex field; e) slightly different formulation of the design problem; f) solution obtained for boundary conditions given in Fig. 1e; g) yet another example of solution to the problem from Fig. 1e obtained for different values of border parameters.

selecting and assembling the component fields in its antisymmetric half is illustrated in Fig. 1d. In the flanges, fields of "s10" type are applied, which determine the shape and dimension of the elements. In order to transfer the forces **S**, and to satisfy the boundary conditions on the borders of oblique elements "s10", it was necessary to introduce oblique webs, in which one applies the fields of the "Ts" type that realise pure sheer. Considering equilibrium conditions on the borders joining the two fields, and assuming thickness of the oblique webs to be $g = 1.8$ [mm], one obtains the thickness of the flanges, $g = 2$ [mm]. In the web with holes one assumes a zero state of stress with fields of type "Ns1" and thickness $g = 2$ [mm].

Another illustrative example of formulation of design problem is presented in Fig. 1e, and two of its solutions, obtained for different values of border parameters, are shown in Figs. 1e and 1f. These solutions are denoted, respectively, "F92b" and "F10". The method of constructing such fields is described in works [3, 4].

2. Computational models

In the FEM analyses performed with the use of the CosmosM software package, we assumed, among other things:

- Small strains and linear-elastic physical model of material.
- Triangular shell elements type SHELL3 with 3 nodes and 6 degrees of freedom in a node.
- The average size of an element 3–5 times greater than its thickness.
- Loads introduced into the models in the form of torsional moments produced by forces Fy applied to the borders of holes in additional diaphragms "p1" (see Figs. 2a, 3a, and 5a); the nodes lying on the borders of holes in the additional diaphragms "p2" deprived of possibility of displacements Uy; fixed displacements Ux, Uy and rotations Ry, Rz of nodes lying in the centre of these diaphragms in order to exclude the possibility of rigid motion.
- The value of load equal to a half of the limit load-carrying capability assumed in the design with the yield point of $\sigma_Y = 300$ MPa; this means that, assuming ideal equalization of equivalent stress level, the equivalent stress would be equal to $\sigma_{eq} = 150$ MPa at each point of the analysed structure.
- The shapes and dimensions of the analysed models are almost ideally consistent with those from the solutions to the design problems; small corrections were only made in the vicinity of contour refractions, which were smoothed with Bezier curves drawn out of the original borders in order to prevent diminishing the assumed limit load-carrying capability [2]; the tasks of border correction have not been undertaken.

The assumed shell model allows only for approximate analysis of local three-dimensional states that arise, for example, in the areas of connection between plane component elements.

In this work, we restrict ourselves to the analyses of only the linear-elastic range of stress, because this is the typical exploitation range in this class of structures. The FEM analyses in elastic-plastic range will be the subject of a separate work.

3. General results of analyses

At the beginning, to facilitate reviewing main results of this investigation, we here summarize the conclusions, which seem to be the general as they frequently appear in the whole range of the already performed analyses:

1. Deformations remain small and membrane states dominate in the structure; equivalent stresses that arise due to bending states take relatively small values.
2. Stress concentrations are low, maximal values of equivalent stresses reach similar levels in all component elements.
3. Good equalization of equivalent stress fields in large fragments of the structures [11], and – in the case of structures built of elements bent in their planes – at least along free borders.
4. Strength properties of structures designed with the SADSF method are radically better than those of systems whose structures were not properly accommodated for the carried load and/or were designed with an intuitive approach.

4. Detailed results

The results are presented as object drawings which illustrate first the important details of the structures and shapes of the models resulting from the solutions to the design problems, and then distribution of equivalent stresses σ_{eq} (in the Huber-Misses sense) arising due to membrane and bending states.

4.1. Model based on solution "F95b"

The shape of the analysed model of the structure "F95b" and the assumed boundary conditions are presented in Fig. 2a.

As it results from the SADSF solution, in the plane ASym of the structure there are no reactions acting perpendicularly to this plane, so that bimoment does not appear there. However, the bimoment arises out of the ASym plane and its value increases with the distance from the symmetry plane reaching a maximum at points where oblique webs are fixed. Then, the bimoment value

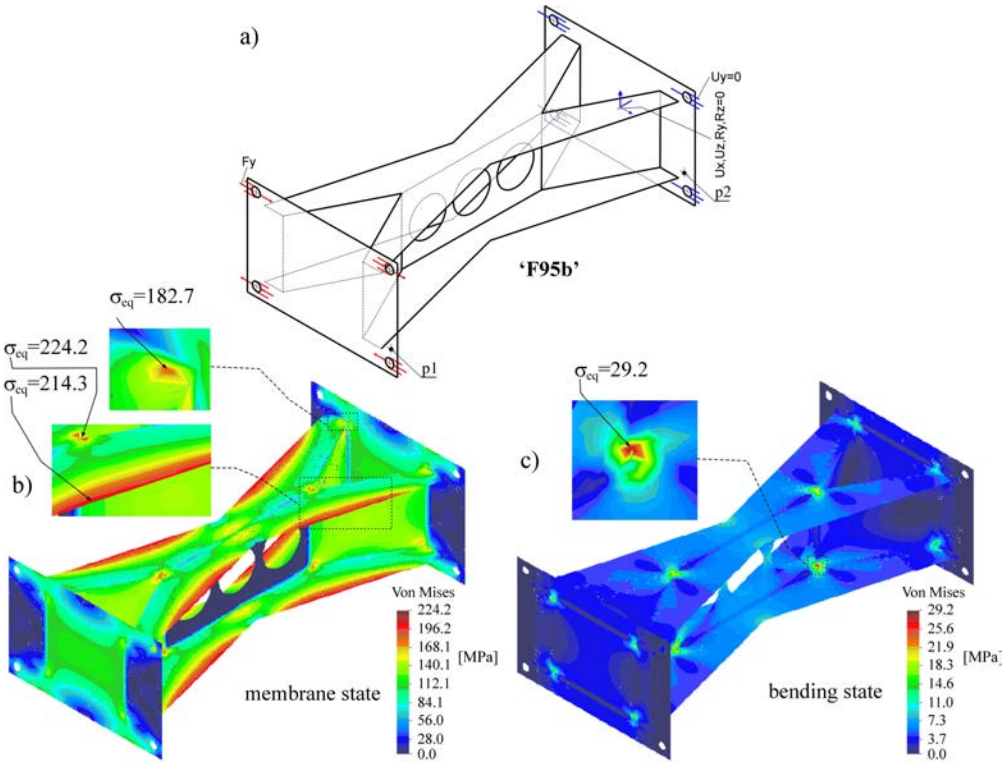

Fig. 2. Shape and boundary conditions assumed for model "F95b" in FEM analyses (a) and distributions of equivalent stresses calculated according to Huber-Misses criterion (b, c)

decreases and drops to zero in the terminal cross-sections of the diaphragms. It is worth noting that, in the vicinity of cross-sections with maximal bimoment values, there also appear the greatest stress concentrations in elastic state.

The distributions of equivalent stresses for membrane and bending states are presented in Fig. 2b and 2c. In Fig. 2b, we can see that:

- There appear small, local concentrations of equivalent stress at different places of the structure (i.e. at points marked with arrows, where $\sigma_{eq} = 224.2$ [MPa], $\sigma_{eq} = 214.3$ [MPa], and $\sigma_{eq} = 182.7$ [MPa]), however, the values of stresses at these points do not significantly differ from one another.
- Good equalization of equivalent stress along free borders of the flanges.
- An almost ideal level of stress equalization in oblique webs, where shearing stress has been assumed in the statically-admissible fields.
- Low equivalent stress areas are observed in the central web (with holes) where a zero state of stress has been assumed.

Consequently, in Fig. 2c one can see that maximal equivalent stress associated with bending state of stress reaches small values, and its maximal value equals only 13% (29.2/224.2) of the value of maximal stress associated with membrane state.

4.2. Model based on solution "F92B"

In the case of the structure model type "F92b", the shape and dimensions assumed for FEM analyses (Fig. 3a) were exactly the same as those obtained from the SADSF design problem (Fig. 1f). Modifications were only applied to the arrangement of holes in the web, for which a zero state of stress was assumed in the SADSF solution, and the web itself was introduced only to retain the constraints that maintained geometry of the structure.

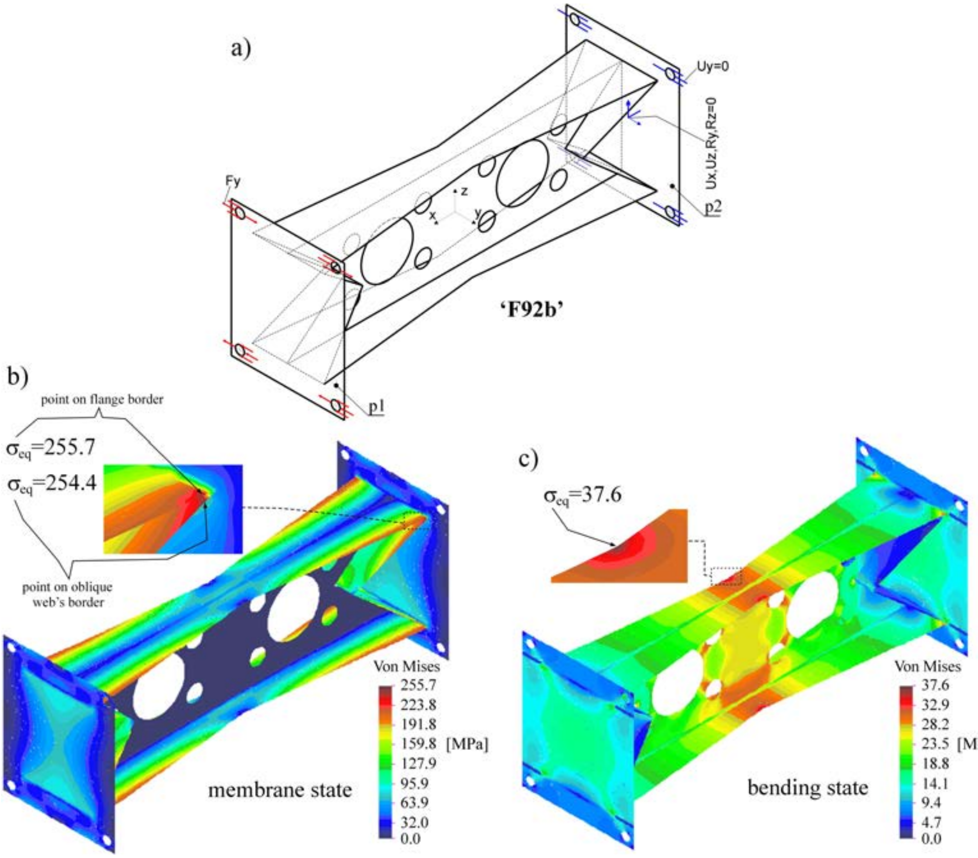

FIG. 3. Shape and boundary conditions assumed for model "F92b" in FEM analyses (a) and distributions of equivalent stresses calculated according to Huber-Misses criterion (b, c).

The structure was based on an **I**-section, and the effect of high rigidity was obtained thanks to the addition of oblique elements in the vicinity of the diaphragms. As follows from the analyses of interactions between component fields [3], these elements should be used for closing the bimoment reactions that arise due to asymmetry of the internal forces ASym (Fig. 1f) and increase with the distance from the plane of symmetry of the structure.

In this structure, all the elements (except the web) are kinds of membranes bent in their planes. In such elements, in the elastic range of load, there appears the axis of bending and strains increase with the distance from this axis. Then, one can expect their especially big discrepancies between the limit fields and elastic fields. However, it turned out that this structure exhibits several good properties, also in the membrane state. Among other things, there we have:

- Good equalization of equivalent stress along free borders and an almost identical maximal values of stress both in the flanges and in oblique elements (compare the values marked in Fig. 3b).
- Relatively low concentration of stresses (the maximal equivalent stress of 255.7 [MPa] is not much greater than that which we would obtain assuming ideal equalization of stress in the whole structure, i.e. stress value of 150 [MPa]).
- Areas with very low load in the web, where a zero state of stress was assumed.

Additionally, we found that the membrane state was the dominant one; the maximal equivalent stress due to bending (Fig. 3c) reached 37.6 [MPa], which was approximately 15% (37.6/255.7) of the maximal value obtained for the membrane state (Fig. 3b).

In order to demonstrate the quality of the presented solution, as well as the scale of possible improvements in strength properties resulting from the application of the SADSF method, we performed FEM analyses for a model of a regular **I**-section. The thickness of the sheet metal plates assumed for both models were the same. We also assumed constant width of the flanges, equal to the maximal width determined from statically admissible fields. The central web however, was without any holes, because the weight of the **I**-section model was assumed to be equal to that of the designed model. Boundary conditions are assumed the same as in the SADSF solution, however, the load value is assumed to be 14 times lower to make the maximum level of equivalent stress approximately the same in both models.

The distributions of the total equivalent stress fields obtained for both models are presented in Fig. 4. Such a great difference between load levels in the two models results first of all from the fact that in the structure from Fig. 4b designed with the SADSF method, the carried load mainly produces membrane state of stress, while in the structure from Fig. 4a the transmitted load must produce a bending state of stress which leads to low rigidity of the structure and generally to high level of equivalent stress [3]. In this model, maximal stress arising due

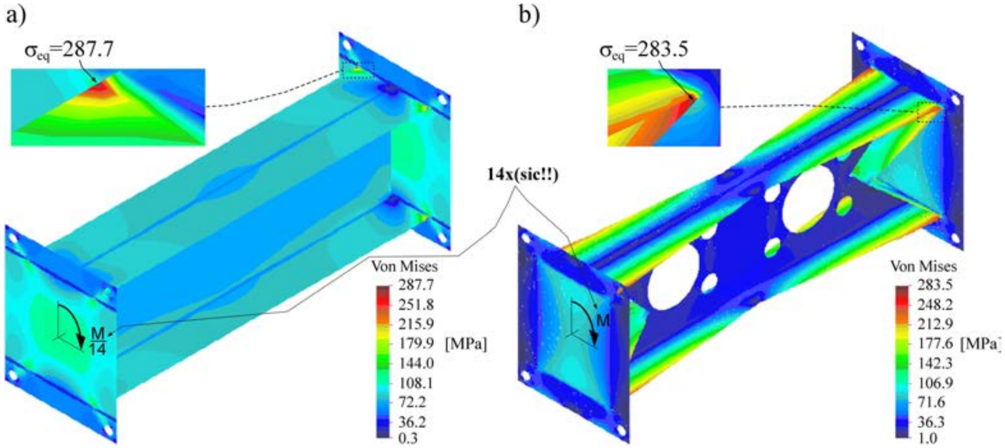

Fig. 4. Example comparison of distributions of total equivalent stresses in the model designed with the SADSF method (b) and in the model based on a regular **I**-section (a).

to membrane state equals 93.4 [MPa], while that associated with bending state is as high as 216.6 [MPa].

4.3. Model based on solution "F10"

The shape of the considered model "F10" and its boundary conditions are well illustrated with the drawings in Fig. 5a. The contour refractions on external borders and the holes in the central web were smoothed with Bezier curves.

This structure is based on a regular channel section, and the effect of high rigidity is achieved by very simple constructional means – by applying two additional plane elements welded into the section in its the central part. Thanks to such a structural design, we managed to "close" self-balancing bimoment systems, and in this way achieve radical increase in global rigidity of the structure as well as a significant decrease in the overall level of stress relative to the loads.

Also in this structure, one can not obtain well-equalized elastic equivalent stress in the flanges and in the additional oblique element because these parts are subjected to bending. In this case, in the membrane state we find (Fig. 5b and 5c):

- Good equalization of equivalent stress along free borders of the flanges.
- Almost the same values of maximal equivalent stresses in the flanges and in the additional oblique element.
- Good conformity between the results of FEM analyses and those of photoelastic examinations. An example juxtaposition of equivalent stress distribution and isochromatic fringes in the upper flange [6] is shown in Fig. 5b.

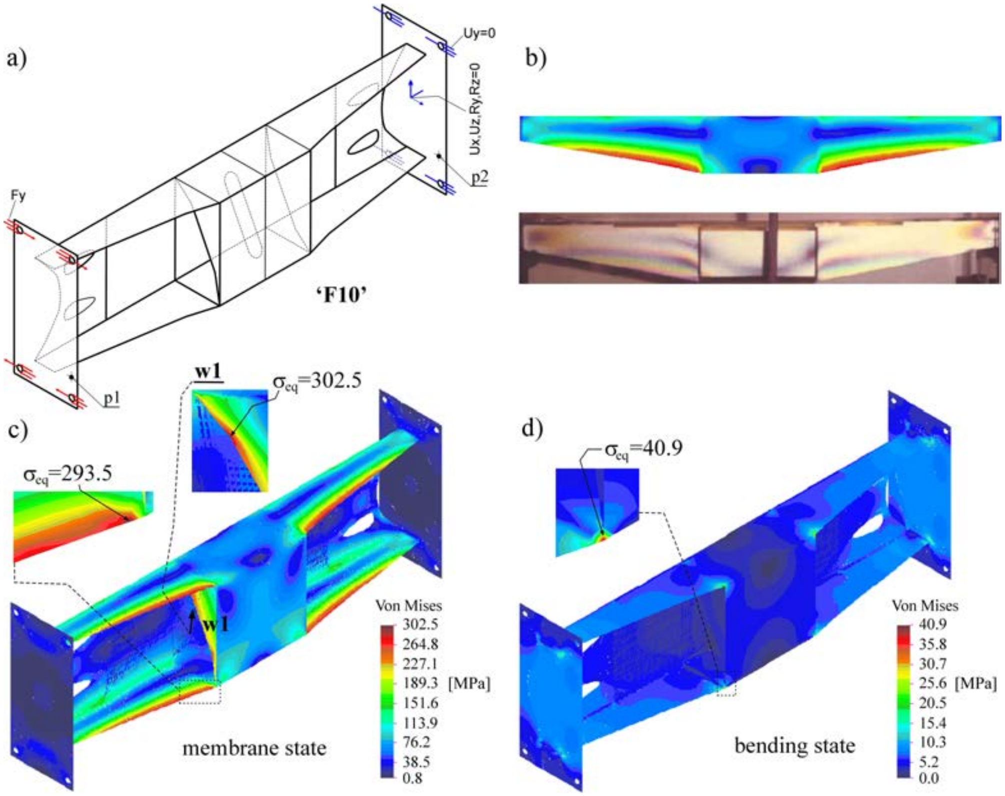

FIG. 5. Shape and boundary conditions assumed for model "F10" in FEM analyses (a), distributions of equivalent stresses calculated according to the Huber-Misses criterion (c, d), and field of isochromatic fringes registered in the flange (b) [6].

The maximal equivalent stress associated with the bending state (Fig. 5b) reaches locally only 14% of the value of equivalent stress related to the membrane state (40.9/302.5).

The essential advantage of systems designed with the SADSF method is that their structures are correctly chosen for the assumed loads, so that the loads are carried by the dominating membrane forces [3, 4]. One may ask however, "What happens if we change the structure obtained from the SADSF solution by removing one of its parts?". Let, for example, this part be the additional oblique element, whose mounting into the structure (by welding) is rather laborious.

This time, however, the load value was assumed 10 times lower in order to obtain the level of equivalent stress similar to that in the SADSF solution.

The distribution of equivalent stresses obtained for such a case is presented in Fig. 6. The bending state is the dominant one, here. Maximal stresses originating from the membrane state are small and constitute just 8.5% of the bending state stresses (28.0/331.9).

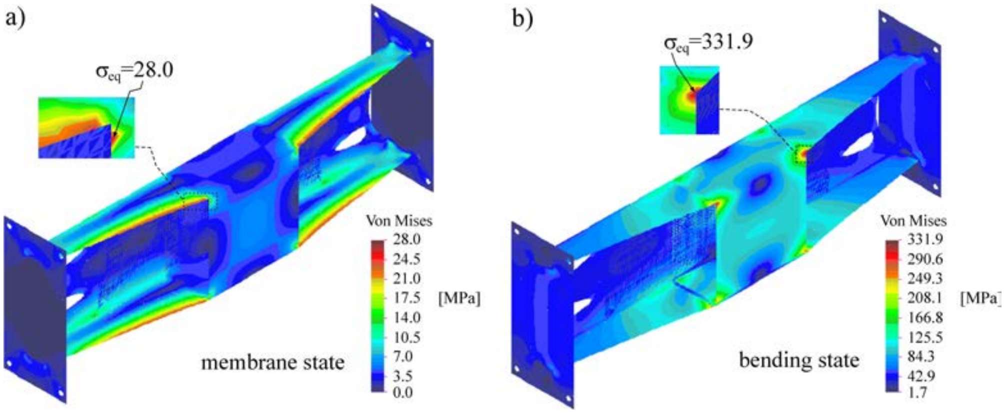

Fig. 6. Distribution of equivalent stresses in the structure modified by removing the additional oblique element and after a ten-fold decrease of the applied load.

5. Conclusions

The results obtained in this study confirm the enormous usefulness of the SADSF method in designing thin-walled structures and justify the need for popularizing this method in industry.

In all the cases analysed already – similarly as in the examples presented in this work – we have always found good and very good strength properties in elastic state. In consequence, the examined structures have also had good properties in the conditions of time-varying loads. Similar conclusions, based on other cases of structures designed with the SADSF method, have been repeatedly published in the relevant literature [2–13].

The scale of the analyses carried-out and the repeatability of the obtained results, allows us to treat the conclusions formulated in this work as general.

The examinations in the elastic-plastic range of stress have shown, among other things, an almost equal limit of load-carrying capabilities of all component elements of the structure, plasticization of vast portions of the structure's volume at the moment of collapse, and the prevalence of the membrane state within the whole range of the load values – up to the value not much smaller than the actual limit load. On the other hand, the collapse itself has always consisted in large, bending-type changes in geometry, and in all cases the actual limit load has turned out to be greater than that assumed in design.

References

1. Bendsoe M.P., Sigmund O., *Topology Optimization: Theory, Methods, and Applications*, Springer, 2003.

2. Bodaszewski W., Szczepiński W., *Shaping structure elements by the method of discontinuous stress fields* [in Polish: *Kształtowanie elementów konstrukcji metodą nieciągłych pól naprężeń*], BEL Studio 2005, PWN, 2006.

3. Bodaszewski W., *Statical analyses and shaping complex thin-walled structures* [in Polish: *Analizy statyczne i kształtowanie brył cienkościennych*], BEL Studio, Warszawa 2013.

4. Bodaszewski W., *Torsioned thin-walled open profiles shaped by the SADSF method* [in Polish: *Skręcane profile cienkościenne o powłokach otwartych, ukształtowane metodą SD-NPN*], Stability of Structures – IX Symposium, 15–20, Zakopane 2000.

5. Bodaszewski W., *The investigation of the models of structural joint shells shaped from the condition of equalized effort in limit state* [in Polish: *Badania modeli powłok węzłów konstrukcyjnych ukształtowanych z warunku wyrównanego wytężenia w stanie granicznym*], 16th Symposium on Experimental Mechanics of Solids, 31–34, Jachranka 1994.

6. Bodaszewski W., Markiewicz I., *Experimental investigations of structural elements shaped by the SADSF method* [in Polish: *Badania doświadczalne elementów konstrukcyjnych ukształtowanych metodą nieciągłych pól naprężeń*], Raport CPBR 4.3 (Etap V), IMBiGS, Warszawa 1989.

7. Dietrich L., Miastkowski J., Szczepiński W., *Limit analysis of structural elements* [in Polish: *Nośność graniczna elementów konstrukcji*], PWN, Warszawa 1970.

8. Frąckiewicz H., Szczepiński W., Tereszkowski Z., Szlagowski J., Bodaszewski W., Trela S., Barchan A., *Joints and structural connections* [in Polish: *Węzły i połączenia konstrukcyjne*], WNT, Warszawa 1986.

9. Markiewicz I., Bodaszewski W., Glinka G., *Global and local design method for fatigue resistant structure*s, SAE 2003 Transactions, Journal of Materials and Manufacturing, Section 5–112, 467–477, 2003.

10. Markiewicz I., *Analysis of elastic effort fields in truck frame designed by the SADSF method*, Eksploatacja i Niezawodność – Maintenance and Reliability, **34**, 2, 22–27, 2007.

11. Markiewicz I., *Analysis of elastic properties of thin-walled structures designed by SADSF method*, Engineering Transactions, **57**, 1, 35–43, 2009.

12. Szczepiński W., *Plastic design of machine parts* [in Polish: *Projektowanie elementów maszyn metodą nośności granicznej*], PWN, Warszawa 1968.

13. Szczepiński W., Szlagowski J., *Plastic Design of Complex Shape Structures*, Ellis Horwood & PWN, Warszawa – Chichester 1990.

14. Web page, www.sadsf.net (Bodaszewski W.).

Received October 29, 2012; revised version March 6, 2013.

ENGINEERING TRANSACTIONS • *Engng. Trans.* • **61**, 2, 151–160, 2013
Polish Academy of Sciences • Institute of Fundamental Technological Research (IPPT PAN)
National Engineering School of Metz (ENIM)

Loosening Evaluation of Bolt-Nut Fastener Under Transverse Cyclic Loading

Naoya NISHIMURA1), Katsuhiko MURASE1), Toshio HATTORI2),
Takeru WATANABE3)

1) *Meijo University, Department of Vehicle and Mechanical Engineering*
1-501 Shiogamaguchi, Tempaku-ku, Nagoya 468-8502, Japan
e-mail: nisimura@meijo-u.ac.jp

2) *Gifu University, Department of Mechanical and Systems Engineering*
Gifu 501-1193, Japan

3) *Meijo University, Graduate School of Science and Technology*
Nagoya 468-8502, Japan

In this paper, we evaluate the sliding and the loosening behavior of thread joints (M16 bolt-nut fastener) under transverse loading. First, the critical relative slippage (Scr), less than the displacement in which the thread joints can keep the fastening, are obtained by the cyclic loading tests. Then, this critical relative slippage is estimated according to the theoretically obtained equation by considering the bending deformation of bolt and the geometrical constraint condition. The inclination compliance (kw) of the bolt head used in this equation is evaluated by comparing the experimental result with the corresponding analytical one. In consideration of the nonlinearity of kw with respect to the bolt axial tension, the Scr is well estimated by this equation.

Key words: thread joint, bolt-nut fastener, sliding and loosening behavior of bolt, transverse loading, critical relative slippage, inclination compliance of bolt head.

1. Introduction

Considering the efficient productivity and maintainability, most of machine and product has many joints (e.g., fastening, welding and adhesive joints). In particular, the thread joint has been frequently used for these purposes as a machine element. However, many troubles, such as loosening of bolted joints or fatigue failure of a bolt, are often experienced. Much attention must be paid to the improvement of the strength and the reliability of the thread joints. It is generally said, that the fastening axial force rapidly decreases by the rotation loosening of nuts if the relative slippage on the interfaces between the nuts and the fastened body goes beyond a certain critical limit [1, 2]. For example, the thermal expansion due to temperature change between jointed members may cause this kind of problem. Another reason for these troubles is that the deformation behavior and strength of the machine are not evaluated sufficiently in the CAE analysis, because of imperfections in the database of mechanical properties of these joints.

The aim of the present research is to construct an industrially available database, including equivalent rigidity and critical relative slippage of these joints for the CAE process. As the first step, in this paper, we present the investigated results of the sliding and the loosening behavior of thread joints (M16 bolt-nut fastener) under the transverse cyclic loading condition. Further, the critical relative slippage (Scr) that prescribes the upper limit for preventing the loosening behavior is experimentally obtained from cyclic loading test. And the inclination compliance (kw) that represents the pseudo-rigidity of the bolt head portion is evaluated using the theoretically constructed equation and the experimental result.

2. Sliding behavior of the thread joint

The sliding behavior of the thread joint under transverse loading is shown in Fig. 1. The deformation behavior of the thread joint mainly depends on the amount of transverse loading given to the joint. When the load is low, the bolt and fastened components (two plates) are deformed as one body (Fig. 1a).

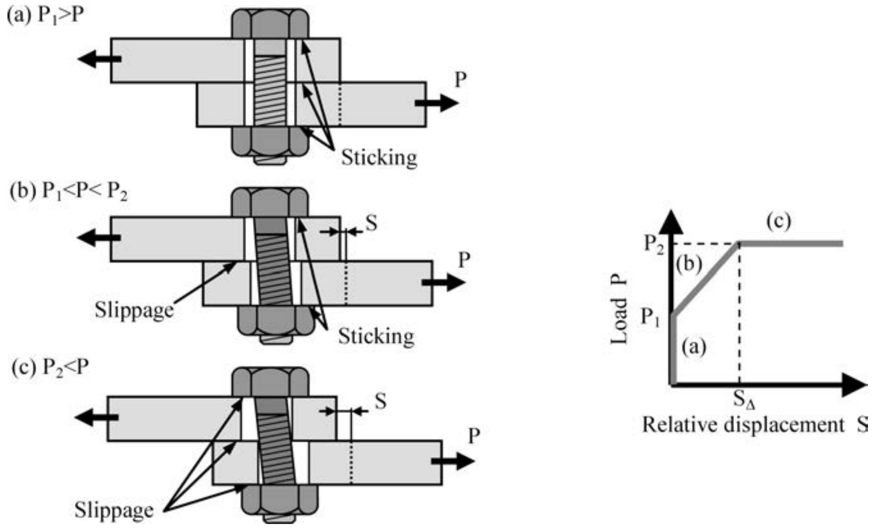

FIG. 1. Behavior of the thread joint (bolt-nut fastener) under different load conditions.

On the other hand, relative sliding is generated at the interface between the upper and lower plates, when the load becomes greater than the frictional force (the number of the bolts $n\times$ the friction coefficient $\mu\times$ the initial bolt axial tension F). However, when relative slippage S between upper and lower plates is small, the relative slippage is absorbed by the bending deformation of the bolt and does not generate the relative sliding between the bolt head and the fastened component (Fig. 1b). The relative displacement increases with the increase in the load. The relative sliding is generated at the interface between bolt head and fastened component, when the relative displacement exceeds the critical relative displacement S_Δ (Fig. 1c). Then, the bolt loosening due to its rotation is inevitable and thus the axial tension decreases.

3. CRITICAL RELATIVE SLIPPAGE SCR

Concerning the loosening of the thread due to its rotation under transverse loading, YAMAMOTO and KASEI *et al.* proposed an equation which evaluates the critical relative slippage using the experimental result [3, 4]. Critical relative slippage Scr that prescribes the upper limit for preventing the loosening behavior is dominated by flexural rigidity of the bolt and the inclination compliance kw that represents the pseudo-rigidity at the bolt head portion. The Scr is estimated by the following equation, which is derived from the bending deformation of the simple beam instead of from the bolt [5]; as shown in Fig. 2. The Scr value is proportional to the bolt axial tension.

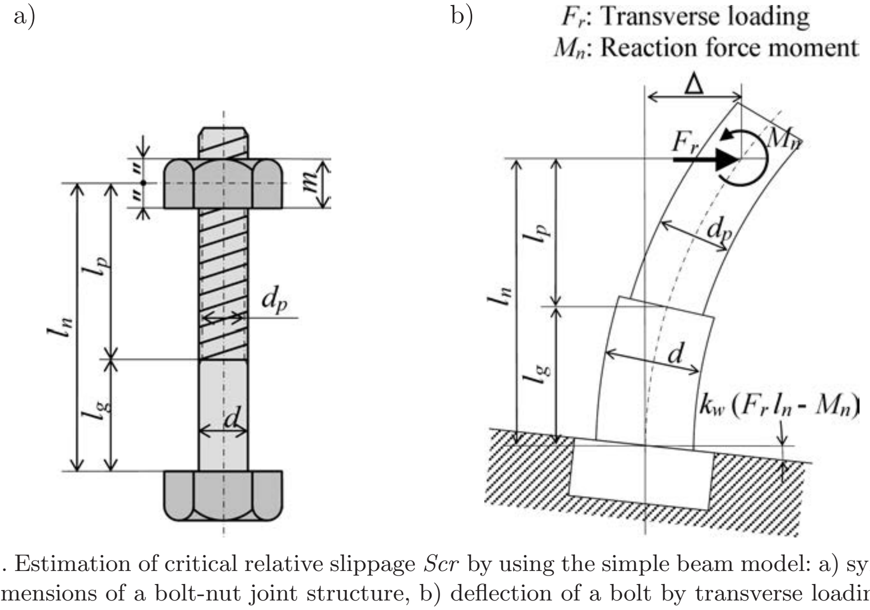

FIG. 2. Estimation of critical relative slippage Scr by using the simple beam model: a) symbolic dimensions of a bolt-nut joint structure, b) deflection of a bolt by transverse loading.

$$Scr = 2\Delta = 2F\left[\mu_w\left(\frac{l_g^3}{3E_bI_g}+\frac{l_p^3}{3E_bI_p}+\frac{l_gl_pl_n}{E_bI_g}+k_wl_n^2\right)\right.$$
$$\left.-\left(\frac{m}{4}\right)\left(\frac{\mu_s}{\cos^2\alpha}\right)\left(\frac{l_g^2}{2E_bI_g}+\frac{l_p^2}{2E_bI_p}+\frac{l_gl_p}{E_bI_g}+k_wl_n\right)\right], \tag{3.1}$$

F – Bolt axial tension, μ_w – frictional coefficient of the interface between bolt head and fastened component, μ_s – frictional coefficient of the threaded interface, kw – inclination compliance of the bolt head portion, E_b – longitudinal modulus of elasticity of the bolt, I_g, I_p – moment of inertia of the cross-sectional area of the bolt, α – half-thread angle, $\cos 2\alpha = 0.75$.

4. EXPERIMENTAL CONDITIONS

4.1. Bolt-nut fastener

Flat plates made of medium carbon steel were fastened with one bolt as illustrated in Fig. 3. The plate has a 64 mm width, 157 mm length and 9 mm thickness. Both plate surfaces were ground in the loading direction. The commonly used bolt made of carbon steel was used for the fastening, whose specification was M16×2(pitch)×55(nominal length) and thread length 40 mm. The specifications of the M16 bolt are given in Table 1. The thread joint and sensors are also shown in the figure. The bolt axial tension is measured by the strain gauge embedded in the bolt.

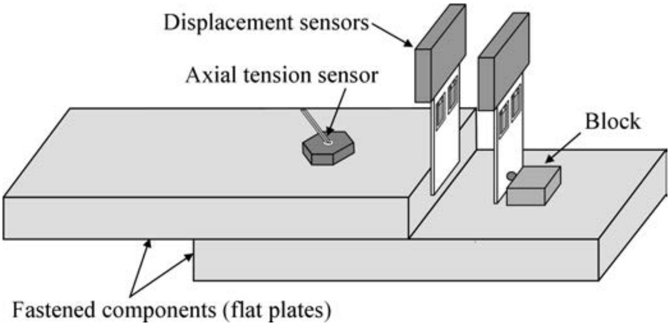

FIG. 3. Bolt-nut fastener and sensors.

Table 1. Specifications of M16 bolt.

Nominal diameter [mm]	Strength classification	Ultimate tensile strength [MPa]	Proof stress [MPa]	Pitch [mm]	Effective sectional area [mm^2]	Standard axial tention [kN]
M16	4.8	392	314	2	157	34.5

4.2. Experimental setup and procedure

The fatigue testing machine with a hydraulic cylinder was used in order to give transverse cyclic loading in the bolt axis direction. The apparatus was composed of a hydraulic pump, servo valve, servo controller, function generator, load cell, and recording device.

Quasi-static or cyclic transverse load was applied to the bolt-nut fastener as shown in Fig. 3. Transverse load, bolt axial tension and displacement of two plates were measured by sensors and a load cell. The displacement of the lower plate was measured by using small block bonded to it. The relative displacement between the plates was also measured.

In the quasi-static loading test, the static loading (tension) was given to the bolt-nut fastener which were fastened by various bolt axial tension (5 types of 35 kN, 30 kN, 25 kN, 20 kN, and 15 kN). The critical transverse load in which sliding was generated between the bolt head and the fastened component was examined.

The cyclic loading (tension-compression) test was carried out. The bolt axial tension was the same condition as the quasi-static loading test. The sinusoidal wave load (displacement) of 1 Hz was applied to the bolt-nut fastener, at most 10,000 times. When the decrease in the bolt axial tension became rapid, the cyclic loading was stopped. The displacement given to the bolt-nut fastener was changed in accordance with the bolt axial tension in order to obtain a critical relative slippage Scr, less than the displacement in which the thread joints can keep the fastening.

5. EXPERIMENTAL RESULTS

5.1. Quasi-static loading test

The relationship between the load and relative displacement of a pair of plates is shown in Fig. 4. In result of the tension loading, the difference between the various bolt axial tensions was compared. It is clear that the lower the bolt axial tension, the lower the transverse load which generates sliding at the interface between the bolt head and fastened component in Fig. 4. The friction coefficient of thread joints used in this research was about 0.19.

The relative displacement that is the relative sliding length was monitored by the displacement sensors during experiment as shown in Fig. 3. When the sliding length increases without an increase of tension, the slippage at the interface between bolt head and fastened component takes place as shown in Fig. 4. This is the critical relative displacement and corresponds to a transition point from a sticking to a sliding condition. It is however difficult to measure it precisely, because a small change in experimental conditions affects much of the result. In

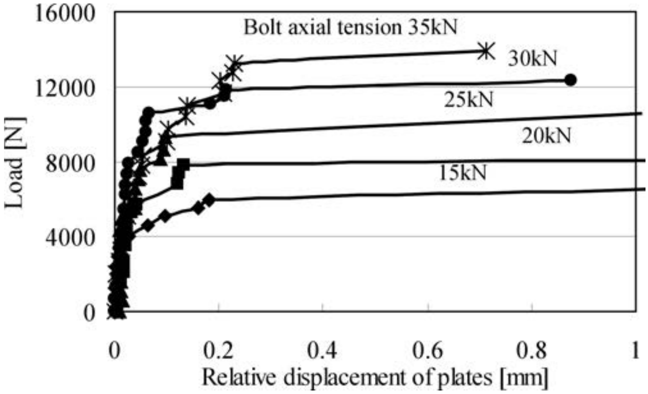

FIG. 4. Dependence of transverse load on relative displacement.

this study, the change of bolt axial tension by cyclic loading was examined, and the critical relative slippage Scr under which the thread joint can keep fastened was obtained from the relation between the amplitude of the displacement and bolt axial tension in cyclic testing.

5.2. Cyclic loading test

The bolt axial tension decreases with the number of cycles as shown in Fig. 5, for various displacement conditions in which the initial bolt axial tension is 15 kN. The decreasing speed in the axial tension is estimated as $\mathrm{d}F/\mathrm{d}N$. The $\mathrm{d}F/\mathrm{d}N$ value was calculated by the change in the bolt axial tension in the range from 500 to 1000 cycles in which the bolt axial tension is regarded as almost linear in all experiments.

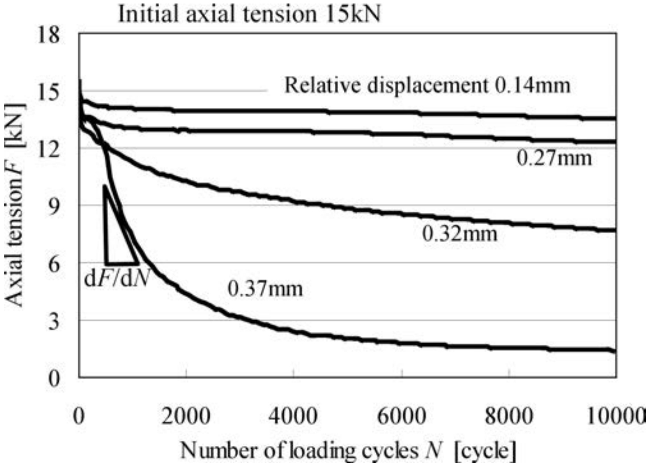

FIG. 5. Dependence of axial tension on the number of loading cycles.

The bolt axial tension decreases rapidly as the relative displacement becomes larger, where loosening of the bolt due to its rotation occurs. The loosening speed of the bolt depends on the number of loading cycles and relative displacement.

In order to determine the critical relative slippage Scr, the loosening speed $\mathrm{d}F/\mathrm{d}N$ with the relative displacement is drawn in Fig. 6 for each bolt axial tension. The relative displacement Scr, at which the loosening speed drastically changed, was determined and whose value is depicted in the figure.

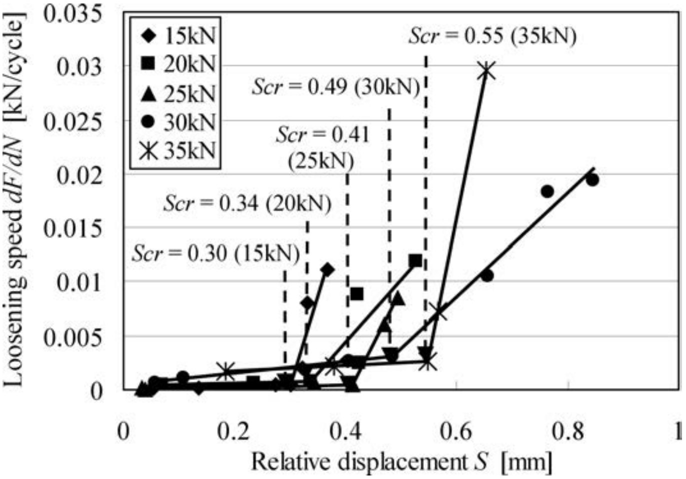

FIG. 6. Dependence of $\mathrm{d}F/\mathrm{d}N$ on the relative displacement.

By substituting the determined Scr in Eq. (3.1) for the case with a bolt axial tension of 35 kN, the inclination compliance kw of the M16 bolt head is calculated to be 3.94×10^{-5} $(\text{kN}\cdot\text{mm})^{-1}$. However, the lower the bolt axial tension becomes, the larger the value of kw varies, because of the decrease of the apparent or equivalent rigidity of the thread joint. In the low fastening force region, the contact surface pressure at the threaded interface and the interface between the nut and the fastened component decreases, and then the bolt head tends to incline. The contact surface pressure over a certain value is necessary such that the constraint force at the thread interface becomes sufficient to avoid the inclination of the bolt. The Scr value is proportional to the bolt axial tension F, such that kw takes on a constant value in the high fastening force region [4]. On the other hand, it was reported that kw was inversely proportional to the bolt axial tension F in the low fastening force region, and took the constant value over some fastening force [6]. The behavior of the bolt screwed to the thick plate where the nut was not used was investigated in these papers. Therefore this estimation method was applied to the bolt-nut fastener. As for the thread joints used in the experiment, the kw of M16 bolt head was evaluated by the following equations, as demonstrated in Fig. 7.

$$kw = (84.4/F) \times 10^{-5} \ \ (\mathrm{kN} \cdot \mathrm{mm})^{-1} \qquad \text{for} \quad F < 21.4 \text{ kN}, \tag{5.1}$$

$$kw = 3.94 \times 10^{-5} \ \ (\mathrm{kN} \cdot \mathrm{mm})^{-1} \qquad \text{for} \quad F \geq 21.4 \text{ kN}. \tag{5.2}$$

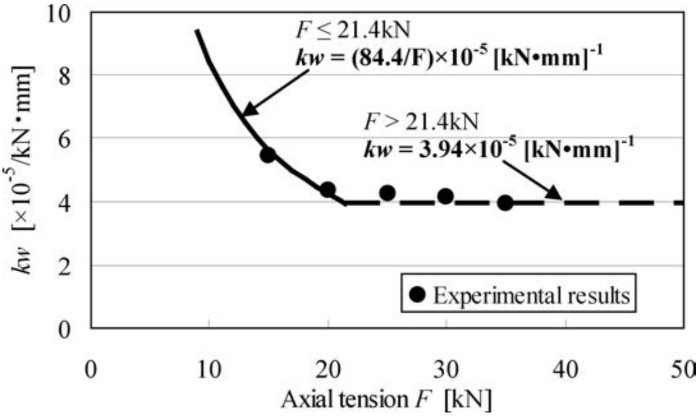

FIG. 7. kw values obtained by experiment and their corresponding fitting curve.

Equation (5.1) is available for conditions with a low bolt axial tension less than 21.4 kN. This bolt axial tension (21.4 kN) shows the minimum value at which kw can be taken as a constant value. Figure 8 describes the two Scr trend lines by Eq. (3.1), in which kw is calculated by Eqs. (5.1) or (5.2). By applying these kw relations, we can estimate the Scr for arbitrary bolt axial tension by Eq. (3.1).

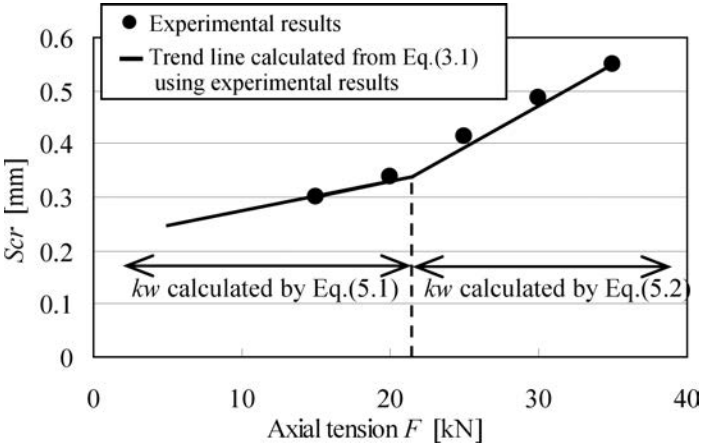

FIG. 8. Estimated Scr by experiment.

In the high fastening force region, it was reported that the *kw* value of the M10 and M22 bolted joint was 1.61×10^{-4} $(\text{kN}\cdot\text{mm})^{-1}$ [4] and 1.4×10^{-5} $(\text{kN}\cdot\text{mm})^{-1}$ [6] respectively. The inclination compliance, which is the reciprocal of rigidity, becomes small, because the rigidity increases with bolt diameter and the bolt head portion does not show the tendency of inclination. The *kw* value of M16 bolt-nut fastener was estimated to be 3.94×10^{-5} $(\text{kN}\cdot\text{mm})^{-1}$ in the present study. Thus the result seems convincing.

These *Scr* and *kw* which are the result in the present study can be applicable as an appropriate deformation threshold of the bolt-nut fastener under the transverse loading condition. The experiment for the various bolt axial tensions and amplitudes of the displacement will be carried out to improve on the accuracy of its value in the future, especially for the transiting bolt axial tension in which *kw* becomes constant.

6. CONCLUSIONS

The transverse loading test for a thread joint (M16 bolt-nut fastener) was carried out, and its sliding and loosening behaviors were examined. The main results are summarized as follows:

1. The critical relative slippage *Scr* less than the displacement, in which the thread joints can keep the fastening, decreases with a decrease of the bolt axial tension.
2. By considering the nonlinearity of inclination compliance *kw* of the bolt head, the critical relative slippage *Scr* is well determined even for cases with low bolt axial tension.

Characteristics for the loosening of various bolt-nut fasteners, including the results of this study, are constructed as an industrially available database and contribute to the accuracy improvement of CAE analysis.

ACKNOWLEDGMENT

This paper was presented at an International Workshop in the year 2011.

REFERENCES

1. JUNKER G.H., *New Criteria for Self-Loosening of Fasteners Under Vibration*, SAE Transactions, **78**, 314–335, 1969.
2. PAI N.G., HESS D.P., *Experimental Study of Loosening of Threaded Fasteners due to Dynamic Shear Loads*, Journal of Sound and Vibration, **253**, 3, 585–602, 2002.
3. YAMAMOTO A., *Principle and design of thread joint*, Yokendo Ltd., Tokyo, 120–127, 1995.

4. Yamamoto A., Kasei S., *Investigations on the Self-Loosening of Threaded Fasteners under Transverse Vibration – A Solution for Self-loosening Mechanism*, Journal of the Japan Society of Precision Engineering, **43**, 4, 470–475, 1977.

5. Izumi S., Yokoyama T., Iwasaki A., Sakai S., *Three-Dimensional Finite Element Analysis of Tightening and Loosening Mechanism of Threaded Fastener*, Engineering Failure Analysis, **12**, 4, 604–615, 2005.

6. Nakamura M., Hattori T., Sato S., Umeki K., *Self Loosening Behavior of Bolted Joints under Transverse Cyclic Loading*, Transactions of the Japanese Society of Mechanical Engineers, **C-64**, 627, 4395–4399, 1998.

Received November 26, 2012; revised version May 5, 2013.

39th Solid Mechanics Conference

September 1–5, 2014
Zakopane, Poland

The series of Solid Mechanics Conferences have been organized by the Institute of Fundamental Technological Research since 1953. The Conferences have maintained high scientific standard and served as a forum for exchange of ideas and research information. A set of invited lectures have been presented at the Conferences by outstanding researchers. The aim of the Conference is to bring together the researchers from different countries and to create them the possibilities for the presentation of scientific results from a wide area of solid mechanics, including the topics:

- biomechanics,
- computational aspects of mechanics,
- continuum mechanics, elasticity and plasticity,
- coupled problems and field theories of solids,
- dynamics of solids and structures,
- experimental mechanics,
- fracture, damage and fatigue,
- geomechanics,
- interfaces, thin layers and contact mechanics,
- mechanics of composites, porous media,
- micromechanics & thermodynamics of materials,
- nonlinear and stochastic dynamics,
- optimization, sensivity and reliability analysis,
- phase transitions and microstructures,
- smart materials and structures,
- structural mechanics.

Oral and poster sessions are planned.
The official language of the Conference is English.

Venue, accomodations, social programme:

As a conference site Zakopane, the fabulous capital of the Polish Tatra Mountains, was chosen. The Conference will be held at the *Hotel Belvedere* (the best hotel in Zakopane), located in the proximity of the town centre with instant access to marked pedestrian routes of the Tatra National Park. A variety of hotels and inns of different standards and prices are located in the vicinity of the Conference Venue. Among the traditionally organized facilities, a Welcome Party, Gala Dinner and excursions are foreseen.

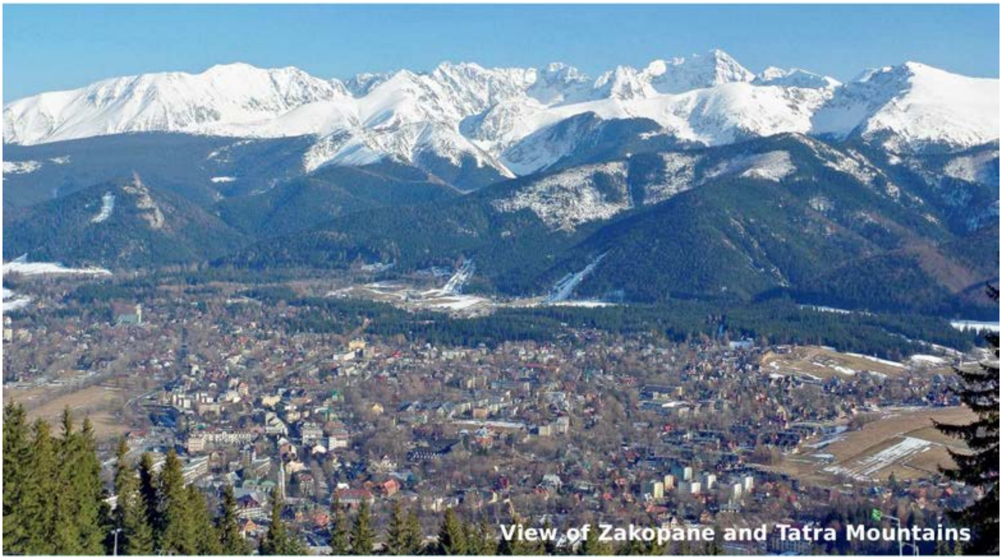

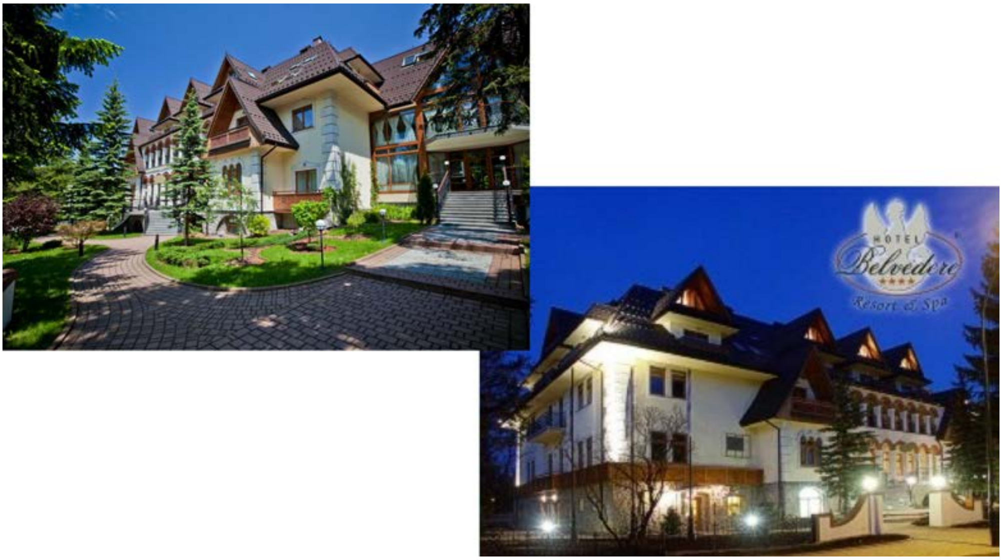

Conference Venue

Scientific Committee:

• Janusz Badur	Institute of Fluid-Flow Machinery, Gdańsk
• Michał Basista	Institute of Fundamental Technological Research, Warsaw
• Adam Borkowski	Institute of Fundamental Technological Research, Warsaw
• Tadeusz Burczyński	Silesian University of Technology, Gliwice
• Paweł Dłużewski	Institute of Fundamental Technological Research, Warsaw
• Witold Gutkowski	Institute of Fundamental Technological Research, Warsaw
• Jan Holnicki-Szulc	Institute of Fundamental Technological Research, Warsaw
• Michał Kleiber	President of the Polish Academy of Sciences, Warsaw
• Witold Kosiński	Polish-Japanese Institute of Information Technology, Warsaw
• Zbigniew Kotulski	Warsaw University of Technology, Warsaw
• Piotr Kowalczyk	Institute of Fundamental Technological Research, Warsaw
• Zbigniew Kowalewski	Institute of Fundamental Technological Research, Warsaw
• Józef Kubik	Kazimierz Wielki University, Bydgoszcz
• Tomasz Łodygowski	Poznań University of Technology, Poznań
• Zenon Mróz	Institute of Fundamental Technological Research, Warsaw
• Andrzej Nowicki	Institute of Fundamental Technological Research, Warsaw
• Piotr Perzyna	Institute of Fundamental Technological Research, Warsaw
• Henryk Petryk	Institute of Fundamental Technological Research, Warsaw
• Ryszard Pęcherski	Institute of Fundamental Technological Research, Warsaw
• Elżbieta Pieczyska	Institute of Fundamental Technological Research, Warsaw
• Wojciech Pietraszkiewicz	Institute of Fluid-Flow Machinery, Gdańsk
• Maciej Pietrzyk	AGH University of Science and Technology, Cracow
• Jerzy Rojek	Institute of Fundamental Technological Research, Warsaw
• Błażej Skoczeń	Cracow University of Technology, Cracow
• Stanisław Stupkiewicz	Institute of Fundamental Technological Research, Warsaw
• Gwidon Szefer	Cracow University of Technology, Cracow
• Jacek Tejchman	Gdańsk University of Technology, Gdańsk
• Andrzej Tylikowski	Warsaw University of Technology, Warsaw
• Krzysztof Wiśniewski	Institute of Fundamental Technological Research, Warsaw

Organizing Committee: Zbigniew Kowalewski – Chairman
Zbigniew Ranachowski – Scientific Secretary

Managing assistants:
Urszula Czubacka
Paweł Grzywna
Dominik Kukla
Tomasz Libura
Agnieszka Rutecka
Jacek Widłaszewski
Joanna Żychowicz-Pokulniewicz

Invited Plenary Lectures:

Holm Altenbach, Germany
Mechanics of Nanostructures

Josef Eberhardsteiner, Austria
Mechanical Behavior of Wood – a Bridge from Microstructure to Structural Applications by Means of Computational Methods

David Hayhurst, UK
High-temperature Continuum Damage Mechanics. Simulation of Materials and Components from Processing and Manufacture to Component Performance

Shuichi Miyazaki, Japan
Development and Deformation Mechanism of Ti-based Shape Memory Alloys Including Gum Metal

Nobutada Ohno, Japan
Homogenized Elastic-Viscoplastic Behavior of Anisotropic Open-Porous Bodies

Ryszard Pęcherski, Poland
Plastic Flow and Failure of Solids. Modelling Across Scales

Krzysztof Wiśniewski, Poland
Recent Improvements in Mixed/Enhanced Shell Elements with Drilling Rotation

Ramon Zaera Polo, Spain
Deformation of Dynamically Phase Transforming Metals in Adiabatic Conditions: Thermal Effects and Instabilities

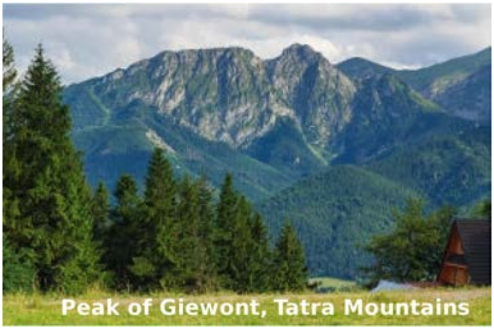
Peak of Giewont, Tatra Mountains


Morskie Oko Lake

Further informations & guidelines will be available at the Conference site:
www.solmech2014.ippt.pan.pl

DIRECTIONS FOR THE AUTHORS

The periodical *ENGINEERING TRANSACTIONS (ROZPRAWY INŻYNIERSKIE)* presents original papers which should not be published elsewhere.

As a rule, the volume of a paper should not exceed 40 000 typographic signs. The following directions are particularly important:

1. **The paper submitted for publication should be written in English.**
2. The title of the paper should be as short as possible. The text should be preceded by a brief introduction; it is also desirable that a list of notations used in the paper should be given.
3. Short papers should be divided into section and subsection, long papers into sections, subsections and points. Each section, subsection or point must bear a title.
4. The formula number consists of two figures: the first represents the section number and the other the formula number in that section. Thus the division into subsections does not influence the numbering of formulae. Only such formulae should be numbered to which the author refers throughout the paper. This also applies to the resulting formulae. The formula number should be written on the left-hand side of the formula; round brackets are necessary to avoid any misunderstanding. For instance, if the author refers to the third formula of the set (2.1), a subscript should be added to denote the formula, viz. $(2.1)_3$.
5. All the notations should be written very distinctly. Special care must be taken to distinguish between small and capital letters as precisely as possible. Semi-bold type must be underlined in black pencil. Explanations should be given on the margin of the manuscript in case of special type face.
6. Vectors are to be denoted by semi-bold type, transforms of the corresponding functions by tildes symbols. Trigonometric functions are denoted by sin, cos, tan and cot, inverse functions – by arc sin, arc cos, arc tan and arc cot; hyperbolic functions are denoted by sh, ch, th and cth, inverse functions – by Arsh, Arch, Arth and Arcth.
7. The figures in square brackets denote reference titles. Items appearing in the reference list should include the initials of the first name of the author and his surname, also the full of the paper (in the language of the original paper); moreover;
    a) In the case of books, the publisher's name, the place and year of publication should be given, e.g., 5. Ziemba S., *Vibration analysis*, PWN, Warszawa 1970;
    b) In the case of a periodical, the full title of the periodical, consecutive volume number, current issue number, pp. from ... to ..., year of publication should be mentioned; the annual volume number must be marked in semi-bold type as to distinguish it from the current issue number, e.g., 6. Sokołowski M., *A thermoelastic problem for a strip with discontinuous boundary conditions*, Arch. Mech., **13**, 3, 337–354, 1961.
8. The authors should enclose a summary of the paper. The volume of the summary is to be about 100 words, also key words are requested.
9. The preferable format for the source file is TeX or LaTeX while MS Word is also acceptable. Separate files for the figures should be provided in one of the following formats: EPS or PostScript (preferable), PDF, TIFF, JPEG, BMP, of at least 300 DPI resolution. The figures should be in principle in gray-scale and only if necessary the color will be accepted.

Upon receipt of the paper, the Editorial Office forwards it to the reviewer. His opinion is the basis for the Editorial Committee to determine whether the paper can be accepted for publication or not.

Once the paper is printed, the issue of Engineering Transactions free of charge is sent to the author.

Also the PDF file of the paper is forwarded by the e-mail to the authors.

Editorial Committee
ENGINEERING TRANSACTIONS